

A TECHNIQUE FOR PASSIVELY COMPENSATING THERMALLY INDUCED  
MODAL DISTORTIONS IN FARADAY ISOLATORS FOR GRAVITATIONAL  
WAVE DETECTOR INPUT OPTICS

By

RUPAL S. AMIN

A THESIS PRESENTED TO THE GRADUATE SCHOOL  
OF THE UNIVERSITY OF FLORIDA IN PARTIAL FULFILLMENT  
OF THE REQUIREMENTS FOR THE DEGREE OF  
MASTER OF SCIENCE

UNIVERSITY OF FLORIDA

2002

Copyright 2002

by

Rupal S. Amin

This thesis is dedicated to my parents and family.

They were always there and never let me back down.

## ACKNOWLEDGMENTS

Acknowledgments are usually a section in a thesis, dissertation, or book that thanks various instructors for their contributions. This section also seems to be the most homogeneous in all books. Well to those people whom I will always call professor, I deliver the following as my version of the acknowledgments.

(Tune of Yakko's "Nations of the world.")

Tanner and Reitze, showed some light, see, although it was infrared,  
had me help correct a laser, and to Guido's pleasure, never found me dead,  
optical alignment, wave confinement, all stored in my head,  
Gouy shifts, higher order rifts, won't let me sleep in bed,  
high work ethics, influenced my kinetics, when talking to Guido (whew),  
and Coldwell kept smiling, 'cause code was compiling, on my CPU,  
Malik was frantic, a CalTech semantic, and helped in afternoons,  
but only in theory, and with a big query, why I never salute,  
Good sir Klauder, your applause get louder, as I add you to my list,  
you showed me tremendously, mainly mathematically, things I had missed,  
Lundock and Guagliardo, the dynamic duo, pushing the physics each day,  
never complained in lab, lined up a slab, and helped me everyday.  
Dr. Jim Simpson, a good physics denizen, taught my first physics class,  
then Dr. Raffalle, got another advisee, from whom physics would pass,  
Drs. Rassoul and Moldwin, won the gold in, geospace science alas,  
they saw I was recruited, and to them I proved, CDVT was not crass,  
Mantovani and Wood, time permitting they should, take Rupal avoidance  
class,

but when I had questions, they would never mention, how I bored  
them and laughed,  
Sawyer, Jin, and Blatt, at a distance they sat, egged me on to do well,  
how they showed me, a bit of arrogancy, does little else but smell,  
Gering I'm sparing, from this poem embarrassing, teaches undergrads who  
dare,  
Paul, TJ, and Nic, whose last names we'll omit, I am sorry for the big scares,  
In high school, there was...Covington, Cloniger, Campbell and Wells, Asher,  
Grover,  
all those teachers who casted their spells,  
and helped me become who I am.  
Also thank you NSF for making this thesis possible.

## TABLE OF CONTENTS

	<u>page</u>
ACKNOWLEDGMENTS . . . . .	iv
ABSTRACT . . . . .	viii
CHAPTER	
1 INTRODUCTION . . . . .	1
1.1 History . . . . .	1
1.2 Gravity Waves . . . . .	3
1.3 Detection of Gravity Waves . . . . .	6
1.4 Faraday Isolators . . . . .	12
1.5 Motivation . . . . .	14
2 THEORY . . . . .	16
2.1 Why Do Materials Absorb EM Energy? . . . . .	16
2.2 Birefringence: Innate and Thermal . . . . .	20
2.3 Magneto-Optics and the Faraday Effect . . . . .	23
2.4 Faraday Isolator . . . . .	28
2.5 Thermal Lens . . . . .	30
2.6 Toy Model and Practice . . . . .	34
2.7 Wavefront Model . . . . .	36
3 EXPERIMENT AND ANALYSIS . . . . .	41
3.1 Design . . . . .	41
3.2 How to Analyze a Thermal Lens . . . . .	42
3.2.1 Scanning Fabry-Perot Cavity . . . . .	42
3.2.2 Beam Profiling . . . . .	52
3.3 Layout of Table . . . . .	53
3.3.1 Table Overview . . . . .	53
3.3.2 Components . . . . .	54
3.3.3 Beam Paths . . . . .	64
3.4 Procedures . . . . .	66
3.4.1 MMT Alignment Techniques . . . . .	66
3.4.2 Overlap Alignment . . . . .	67
3.4.3 Data Collection . . . . .	68
3.5 Absorption Coefficients . . . . .	70
3.6 Analysis . . . . .	71

4	CONCLUSION . . . . .	77
4.1	Results . . . . .	77
4.2	Future Experiments . . . . .	77
APPENDIX		
A	COMPLEX-Q AND THE ABCD LAW . . . . .	79
A.1	Derivation of q . . . . .	79
A.2	ABCD Laws for Gaussian Laser Propagation . . . . .	82
B	JONES MATRICES . . . . .	85
C	UF THERMAL LENSING CODE . . . . .	87
	REFERENCES . . . . .	105
	BIOGRAPHICAL SKETCH . . . . .	108

Abstract of Thesis Presented to the Graduate School  
of the University of Florida in Partial Fulfillment of the  
Requirements for the Degree of Master of Science

A TECHNIQUE FOR PASSIVELY COMPENSATING THERMALLY INDUCED  
MODAL DISTORTIONS IN FARADAY ISOLATORS FOR GRAVITATIONAL  
WAVE DETECTOR INPUT OPTICS

By

Rupal S. Amin

December 2002

Chair: David B. Tanner  
Major Department: Physics

A technique to compensate thermal lenses in next generation gravity wave detector input optics has been studied. For long optics, such as Faraday isolators, the thermal dependence of the index of refraction can be exploited to recover 94 percent of the original  $TEM_{00}$  mode at 50 W of incident light. Theoretical calculations describe the possibility of recovering 95 percent  $TEM_{00}$  light under 200 W of incident radiation when an optimized compensator is used. This level of compensation is demanded since next generation interferometers have stringent specification for input laser mode quality and input amplitude.

## CHAPTER 1 INTRODUCTION

### 1.1 History

$$\vec{F} = \frac{Gm_1m_2}{r^2}\hat{r} \tag{1.1}$$

For nearly three centuries this equation was regarded as absolutely accurate. Withstanding the tests of time, Isaac Newton’s “Law of Gravity” proved itself in numerous earthly experiments and observations. From Galileo’s proposition that bodies fall at the same rate regardless of mass to Kepler’s conclusion that planetary orbits were ellipses in pre-Newtonian times to Hooke and Halley’s debate over planetary orbits, the law of gravity remained unchanged [1]. It was considered infallible, to the point that it was given the title of “The Law of Gravity.”

However strong this model was, problems with the predictions started to surface when people looked more deeply into the sky. The most prominent problem dealt with one of the least visible planets. Mercury’s orbit was found not to be closed. Newton and Kepler predicted and calculated its orbit to be an unchanging ellipse with the Sun at one of the foci [1, 2]. Instead the perihelion was shifting by better than five thousand arcs seconds each century. This posed a dilemma for physics developed in the mid-17th century.

The early twentieth century brought about a change in the model of this force. In an effort to corroborate Michelson and Morley’s null ether experiment, Albert Einstein along with several other physicists constructed a model based on geometrized deformation of space-time [1]. Since this theory handled the world

in what would be called “flat space,” it became known as “special relativity.”<sup>a</sup> The application of Einstein’s theory to general space-time coordinates resulted in the “general theory of relativity.”<sup>b</sup> Nonetheless, the 1916 publication effectively described the interplay between energy and the surrounding space-time [2, 3]. This is what we call gravity.

Nonetheless, the model did not stop at updating Newton’s laws of gravity. The other motivation of GR was to raise the description of gravity to the regime of electromagnetics. Completion of the famed Michelson-Morley experiment showed that the electromagnetic equations written down in the mid-1800s were invariant in the regime of relativistic mechanics [2, 3]. Gravity demanded a model with appropriate relativistic corrections.

Once the foundations of general relativity were laid, investigations into aspects of the gravitational force could begin. Predictions made by GR necessitated a set of realizable experiments. Therefore a series of classical tests both astronomical and Earth-based were devised.

The first of these tests calculated Mercury’s perihelion shift. GR’s exploitation of geometric deviations obtained the correct perihelion shift missed by various parameterized Newtonian theories [1, 2, 3].

Eddington’s famed trek into Principe Island, Africa came second [1]. According to GR, light flows along paths called geodesics. These paths which are ordinarily straight lines in flat space can be curved by massive astrophysical objects. During 1919’s eclipse, Sir Arthur Eddington made observations of the Hyades cluster which was positioned near the solar disk [2, 3]. Predictions and observations

---

<sup>a</sup> The abbreviation SR will be used for special relativity.

<sup>b</sup> The abbreviation GR will be used for general relativity.

disagreed by one degree [3]. This bolstered Einstein's theory at the November meeting of the Royal Society [1].

Following the advent of the nuclear age, the third test used little more than radioisotopes and a convenient five story building. Gamma ray photons climbing out of the Earth's gravitational well displayed a red shift of their frequency. Since the radioactive mass was not in motion, the frequency change was not caused by a Doppler effect. Therefore, the only remaining explanation for the photons losing energy was through gravitational interaction. GR's predictions fell along empirical data as with the previous two experiments [3].

## 1.2 Gravity Waves

Another prediction made by general relativity is the existence of gravity waves [2, 3]. This effect is analogous to what happens when one shakes an electric charge. The surrounding field oscillates and carries energy away from the source in the form of light. Similarly binary orbiting masses, asymmetric supernova, and even the birth of the universe release gravity waves. The prediction can be reconstructed through the following means.

First we assume that an observer is standing in a region of flat space-time. Flat space-time can be represented by a  $4 \times 4$  tensor that appears as

$$\eta_{\mu\nu} = \begin{pmatrix} -1 & 0 & 0 & 0 \\ 0 & 1 & 0 & 0 \\ 0 & 0 & 1 & 0 \\ 0 & 0 & 0 & 1 \end{pmatrix}. \quad (1.2)$$

We add a weak field perturbation,  $h_{\mu\nu}$ , to this flat space-time,

$$\begin{aligned} |h_{\mu\nu}| &\ll 1, \\ g_{\mu\nu} &= \eta_{\mu\nu} + h_{\mu\nu}. \end{aligned} \quad (1.3)$$

Here  $g_{\mu\nu}$  is the metric tensor that expresses the new space-time. We next apply the d'Alembertian,<sup>c</sup>

$$\left(-\frac{1}{c^2}\frac{\partial^2}{\partial t^2} + \nabla^2\right)g_{\mu\nu} = -\frac{16\pi G}{c^4}T_{\mu\nu}, \quad (1.4)$$

where  $G$  is the gravitational constant,  $T_{\mu\nu}$  is the stress-energy tensor, and  $c$  is the speed of light in a vacuum [2, 3, 4]. Originally, the statement called for a nearly flat space-time. This means that we are not near any of the masses represented on the righthand side of the equation. Therefore, we may set the righthand side of the above equation to zero,

$$\left(-\frac{1}{c^2}\frac{\partial^2}{\partial t^2} + \nabla^2\right)g_{\mu\nu} = 0. \quad (1.5)$$

Since the flat space metric,  $\eta$ , is a constant, a derivative operating on it will yield zero. This leaves only the perturbation metric upon which the operator may act,

$$\left(-\frac{1}{c^2}\frac{\partial^2}{\partial t^2} + \nabla^2\right)h_{\mu\nu} = 0. \quad (1.6)$$

The solution to this harmonic differential equation is a harmonic function. Through separation of variables, we find that the harmonic solution takes the form of

$$h_{\mu\nu} = \frac{A_{\mu\nu}}{r}e^{-i(\vec{k}\cdot\vec{r}-\omega t)}, \quad (1.7)$$

where  $A_{\mu\nu}$  is the amplitude of the space-time fluctuation,  $r$  is  $\sqrt{x^2 + y^2 + z^2}$ , and  $\vec{r} = x\hat{x} + y\hat{y} + z\hat{z}$  [2, 4]. The reader will notice the shift to spherical coordinates.  $A_{\mu\nu}$  can be acquired by solving the differential equation inside the source and applying the boundary conditions.

Since the Einstein equations are gauge independent, we can change basis to a transverse traceless (TT) gauge. This provides an additional restriction in the

---

<sup>c</sup> The d'Alembertian is a four space derivative.

number of freedoms used to obtain  $A_{\mu\nu}$  [2, 3]. The TT gauge condition implies that a solution for the z-axis would be

$$A_{\mu\nu}^{TT} = \begin{pmatrix} 0 & 0 & 0 & 0 \\ 0 & A_{xx} & A_{xy} & 0 \\ 0 & A_{xy} & -A_{xx} & 0 \\ 0 & 0 & 0 & 0 \end{pmatrix}. \quad (1.8)$$

This results in a final TT solution for  $h_{\mu\nu}$  being

$$h^{TT\mu 0} = 0, \quad \mu = 0, 1, 2, 3, \quad (1.9)$$

$$h^{TTik} = \frac{2G}{c^4 r} \cdot \left[ \frac{d^2}{dt^2} Q^{TTik} \left( t - \frac{r}{c} \right) \right], \quad i, k = 1, 2, 3, \quad (1.10)$$

where  $Q^{TTik}$  is the traceless transverse quadrupole moment of the source. From inspecting the  $A$  matrix we find that two polarizations exist for gravity waves. These are the “x” and “+” polarizations. This is due to gravity’s monopole nature; there is no “anti-mass.” Since the wave is quadrupole in the lowest order approximation, an asymmetric source is required to produce gravitational waves [2, 3].

Should these waves be detectable then the sources of these waves could be observed. A new field in astronomy based on gravitational waves would extend knowledge of the universe beyond that of the electromagnetic (EM) and particle spectra. Unlike EM waves and cosmic rays, gravitational waves can travel through the universe unimpeded by matter.

A single gravitational wave based telescope would in theory be able to “see” to physical processes that conventional telescopes cannot begin to observe. Processes such as binary star and black hole-black hole mergers, events hidden by nebulae, and events that occurred prior to the decoupling of the microwave background during the birth of our universe would become visible and not left to conjecture.

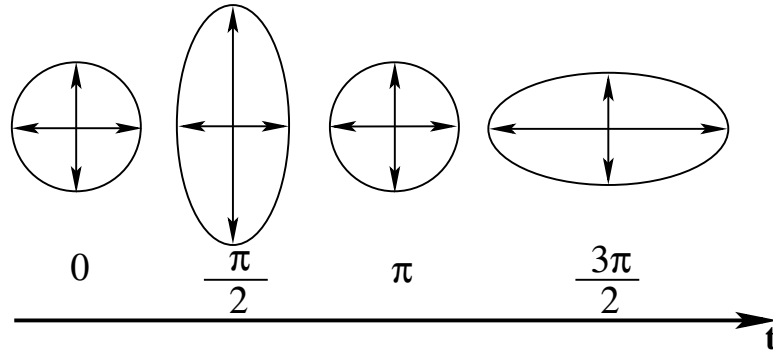


Figure 1–1: The effect of a gravitational wave on a circle. The wave is moving axially to the circle. The circle shows no net displacement. Its perimeter returns to its original shape after  $\pi$  radians.

A single telescope could theoretically see to the edge of our universe, but such a device would be omni directional and would not be able to distinguish events let alone direction. The solution to this problem is the same solution used for particle based telescopes, an array of detectors. An array provides the possibility of coincidence. This scheme first permits verification of the wave and second allows for some directionality.

### 1.3 Detection of Gravity Waves

Now we must examine whether or not these waves are detectable by current technology and physical knowledge. A gravitational wave produces no net movement. Rather it exerts a strain on its medium, the local space-time. As it passes through an object, the object is stretched in one direction and compressed in the orthogonal direction.

The ratio of the change in an object's length to its original length is strain [5] and is written as

$$h = \frac{\Delta l}{l_0}. \quad (1.11)$$

Assuming that the detector is tuned to binary star mergers in the Virgo cluster (20 million parsecs away) [6], one may expect to observe strains of magnitude  $h \sim 10^{-20}$ . In practical terms this is a displacement of one hydrogen atom's

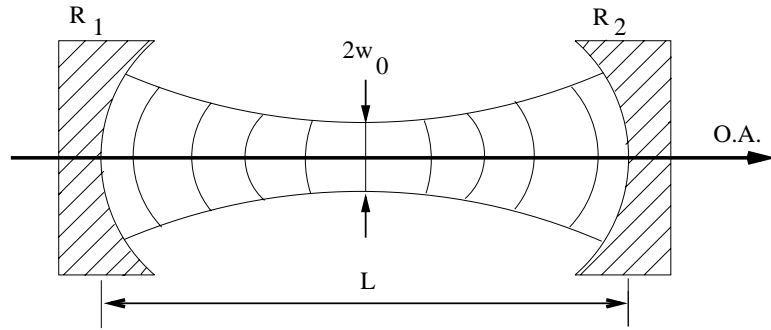


Figure 1–2: A Fabry-Perot interferometer.  $R_1$  is reflectivity of mirror 1;  $R_2$  is reflectivity of mirror 2;  $L$  is the length; O.A. is the optical axis;  $w_0$  is the beam radius. Light enters the device through the left mirror. When on resonance, an interferometer with mirrors of the same reflectivity will transmit all light through the right mirror. In order to sit on the fundamental resonance, the two mirrors must be an integral number of wavelengths apart and possess the same radius of curvature as the impacting light wave.

length over a distance from the Sun to Saturn. However, well-designed optical interferometers can detect displacements of one atomic width on laboratory scales. This ability rises from light’s wave characteristic. A set of coherent light waves out of phase with each other will generate destructive interference reducing the overall output amplitude. Coherent light waves that are in phase will constructively interfere or increase in overall output amplitude.

An estimation shows whether or not interferometers would be a practical solution for strains of this magnitude. We begin with set of estimates for a Fabry-Perot interferometer.<sup>d</sup>

Table 1–1: Hypothetical Fabry-Perot cavity characteristics

Arm length	Reflectivity	Wave Number	Strain
1 m	0.999999	$2 \times 10^7 \text{ m}^{-1}$	$10^{-20}$

---

<sup>d</sup> An interferometer composed of two partially reflective mirrors. These mirrors reflect the light along the optical axis. This results in multiple superimposed beams interfering with each other.

The effective length of the interferometer is  $l_{eff} \sim 10^6$  m. This provides a phase shift of

$$\delta\phi \sim 10^{-7}. \quad (1.12)$$

This is a detectable phase shift [7].

Being a quadrupole wave, gravity waves can be readily detected by a Michelson interferometer. This interferometer is capable of detecting the stretch and compression in both orthogonal directions simultaneously for one polarization. The Michelson functions like the Fabry-Perot through phase differences in wave

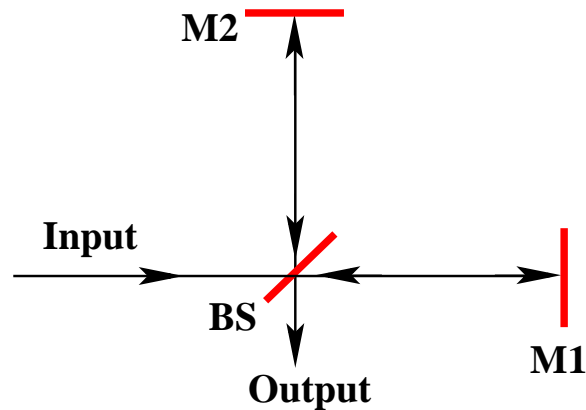


Figure 1–3: A simple Michelson interferometer. BS = beam splitter; M1, M2 = mirrors. Light enters this interferometer and is directed on a beam splitter. The beam splitter creates two beams that reflect off their respective arm mirrors and return to the beam splitter. If the two beams return with their waves in phase the full input power leaves the system through the anti-symmetric port. If the two beams are slightly out of phase, anti-symmetric (output) port will be dimmer than the aforementioned resonant state. When the two beams are  $180^\circ$  out of phase, no light leaves through the anti-symmetric port. Instead it exits the instrument through the input port.

propagating between the end mirrors and the beam splitter. Waves that arrive at the beam splitter after reflection off the end mirror destructively interfere with each other. Waves that return in phase add in constructive interference. Therefore, a Michelson with immovable end mirrors and beamsplitter will be able to observe

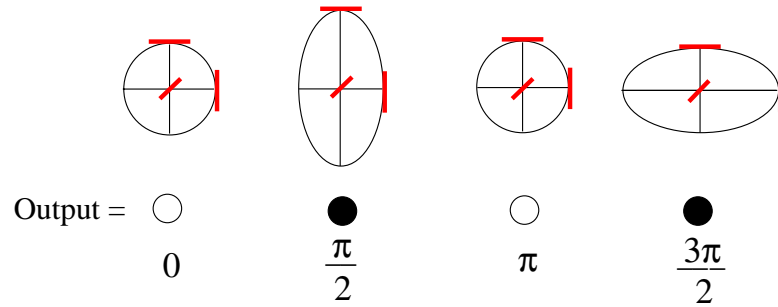


Figure 1–4: A diagram indicating Michelson interferometer output during gravitational wave passage.

the gravity wave as it passes. Making the three interferometer components immovable restricts the number of items that can change the arm lengths to that of the gravity wave.

Being a quadrupole wave, the strain amplitude reaches maximum at one-quarter cycle,  $\pi/2$  and returns to zero displacement at half-cycles,  $\pi$ . For a large scale detector the light must sample this part of the wave. Sampling beyond one-quarter cycle will only average over the detected signal [8]. This will reduce the effectiveness of the detector. Assume that an in-spiraling binary star system were to have a frequency of 300 Hz. We can find the length of the detector arms.

$$\frac{f_g l}{c} \leq \frac{1}{4}. \quad (1.13)$$

where  $f_g$  is the gravitational wave frequency,  $c$  is the speed of light, and  $l$  is the interaction length. The Michelson's arms should be no more than 250 km!

A practical detector with 250 km arm lengths would not be feasible on Earth. However, the phase shift calculation referred to beam folding in a cavity with a much smaller length. Through highly reflective mirrors a 1 m Fabry-Perot may act like a 1 Mm interferometer. Therefore it would be logical to introduce the Fabry-Perot resonance cavities into the arms of a Michelson interferometer.

Another method of beam folding is the delay line. A delay line does not reflect light along the optical axis as does the Fabry-Perot. Rather a single beam

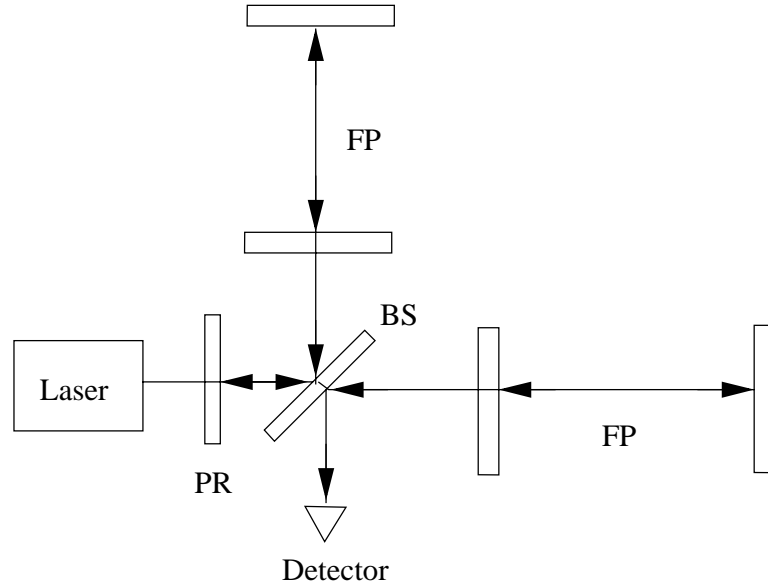


Figure 1–5: This is a simplified schematic of LIGO. PR = power recycling mirror; FP = Fabry-Perot cavity; BS = beamsplitter. Modifications to the Michelson interferometer include a power recycling mirror and a Fabry-Perot cavity in each arm. The power recycling mirror impedance matches the laser light to the interferometer.

bounces a distinct number of times between the two end mirrors before leaving the device [8]. The delay line is not an interferometer by itself; it is a means of using mirrors to increase the total optical path length.

Using these strategies several detectors around the world are being or have been built. Virgo (Italy-France) [9] and GEO<sup>e</sup> (Germany-Britain) [10] are two European detectors with 3 km and 600 m arm lengths respectively. GEO is operational. The US effort named LIGO is composed of three detectors [11, 12]. Two detectors have arm lengths of 4 km and sit in Livingston, Louisiana, and Hanford, Washington. A third detector with 2 km arms also shares the

---

<sup>e</sup> GEO is the only delay line based interferometer.

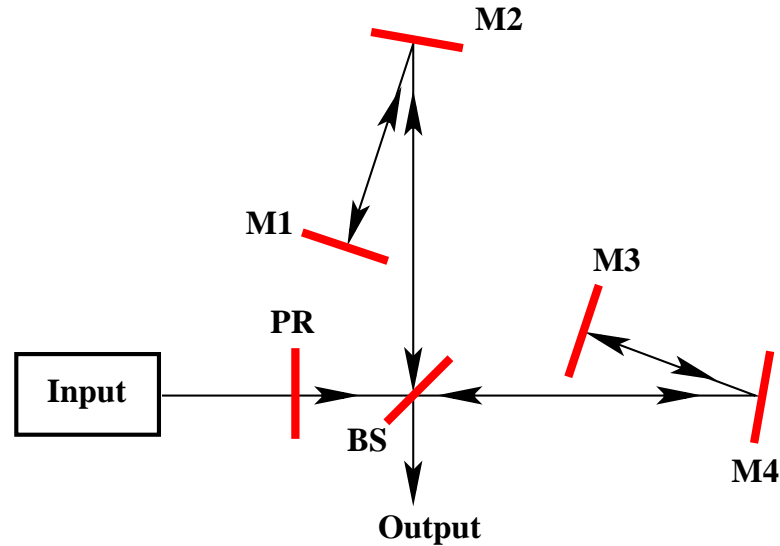


Figure 1–6: A simplified schematic of Germany’s GEO detector, a delay line setup. PR = power recycling mirror; BS = beam splitter; M1, M3 = retroreflectors; M2, M4 = turning mirrors. Light enters GEO’s beam-splitter and is broken into two beams. These beams travel down their respective arms and reflect off the turning and retroreflector mirrors. The beams then re-converge on the beamsplitter where the beams interfere. Notice that the total arm length exceeds the length from the beam splitter to the turning mirrors.

Hanford site. Other prototypes are found in Japan (TAMA300) [13] and Australia (ACIGA<sup>f</sup>).

Detecting such small phase shifts demands extremely clean light sources, lasers, and extremely accurate mirror positioning to reduce any background noise. These tasks have been broken into several parts at LIGO, the pre-stabilized laser, the input optics, core optics—the interferometer itself, suspensions, and data analysis.<sup>g</sup> The pre-stabilized laser comes from a LightWave neodymium doped ytterbium aluminum garnet (Nd:YAG) laser. This laser is cleaned in terms of axial

<sup>f</sup> ACIGA’s Gin Gin site is under construction.

<sup>g</sup> The last two will not be discussed.

frequency and transverse mode to attempt to insure no source induced phase shifts. The laser then enters the input optics.

Input optics' table performs three addition functions beyond beam pointing. Phase modulated sidebands are injected onto the laser, now called the "carrier field." This permits accurate mirror positioning using the Pound-Drever-Hall scheme. Next the laser is cleaned further through the aid of a triangle ring cavity. This cavity permits only the  $TEM_{00}$  spatial mode to pass. All other modes are ejected out of the beamline. The core optics are decoupled from the pre-stabilized laser by a Faraday isolator. Finally, the laser enters a mode matching telescope that accurately focuses (mode matches) to the interferometer.

Once the laser enters the core optics, a correctly mode matched laser will resonate within the 4 km Fabry-Perot arm cavities until the cavities are pushed off their resonant states via a gravitational wave. Since the Michelson component of the LIGO interferometer functions on the dark fringe, completely destructive interference, a passing gravitational wave will generate constructive interference and the output port will brighten.

This last point about the working point of the interferometer is why isolating the core optics from the pre-stabilized laser is important. An interferometer whose output port is dark reflects its optical power upstream. Reflected laser light can easily destabilize an interferometer's sensitive laser source. Effectively the lasing medium will see two laser fields competing for power and thereby generating beats in the output laser light [14]. Faraday isolators guard against this.

#### 1.4 Faraday Isolators

Faraday isolators are based around magneto-optic crystals. The current industry standard is terbium gallium garnet ( $Tb_3Ga_5O_{12}$  or TGG). When used in combination with two polarizers and a half-wave plate, an isolator behaves like

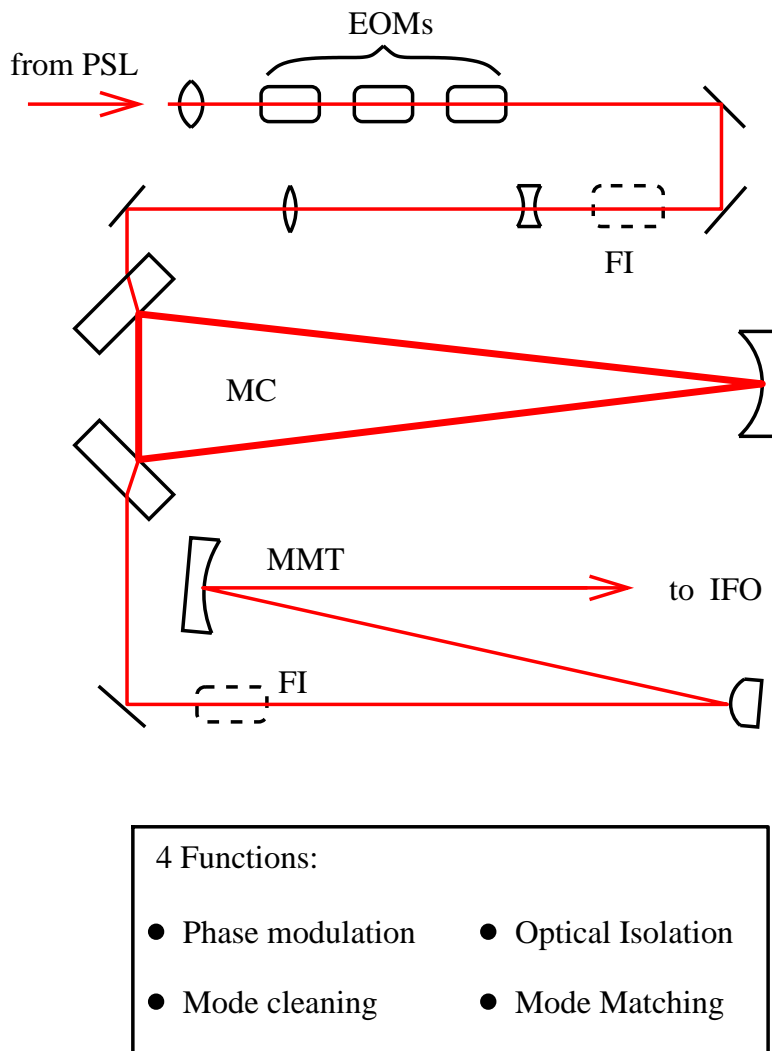


Figure 1-7: A schematic of UF Input Optics table for LIGO II. MMT = mode matching telescope; EOM = electro-optic modulator; PSL = pre-stabilized laser; MC = mode cleaner; IFO = interferometer. Notice the positioning of the Faraday isolator immediately upstream of the mode matching telescope.

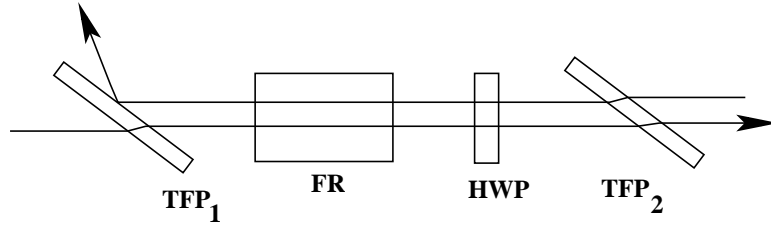


Figure 1–8: A diagram of the Faraday isolator’s internal components. FR = Faraday rotator; TFP = polarizer; HWP = half-wave plate

an electrical diode. Light travelling downstream<sup>h</sup> passes through the device and leaves with the same polarization. Light propagating upstream, however has its polarizations altered and is deflected out of the beamline.

### 1.5 Motivation

Although Faraday isolators protect upstream components from core optic’s reflections their position in the beamline becomes problematic for future gravitational detectors. In order to reduce shot noise<sup>i</sup> and extend the observable range of LIGO, Advanced LIGO designs call for laser power to be increased from 10 W to 200 W. This will heat the magneto-optic crystal. A thermal gradient centered on the laser will generate a “thermal lens” [15, 16, 17, 18, 19, 20]. This lens acts like a gradient-index (GRIN) lens [21]. The accuracy of mode matching into the core optics will degrade, and with less light resonating within the Fabry-Perot arm cavities the LIGO will lose fringe contrast [15, 16, 17, 18, 19, 20].

Therefore, methods must be found to repair this problem of thermal lensing in Faraday isolators. A few techniques are already under consideration. One tactic involves heating the TGG element via a nichrome heater. Materials that are thermally homogeneous possess no thermal gradient and therefore no thermal

---

<sup>h</sup> The terms “upstream” and “downstream” refer to the direction of designed beam propagation.

<sup>i</sup> A noise term due to statistical counting errors.

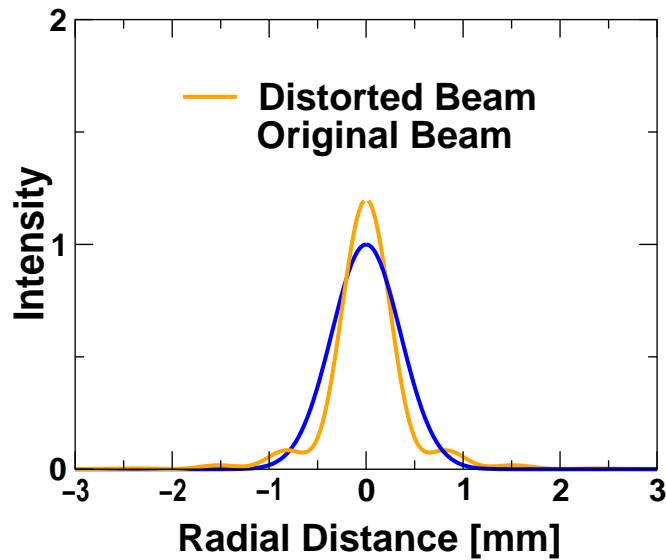


Figure 1-9: A diagram of intensity distortion after a laser passes through a thermal lens. A Gaussian input beam is shown in blue. The orange beam indicates the intensity profile that generated when the Gaussian beam encounters a thermal lens.

lens. A second tactic would use adaptive optical components for the final mode matching telescope. The mirrors of this telescope could be deformed by a second laser whose frequency is absorbed by the mirror substrate. A computer program would determine how to write a deformation into the mirror. Both methods involve active components and active monitoring of the laser's wavefront before delivery to the core optics.

This thesis describes a method for a passive solution that would not require monitoring or adjustment through the full power range of the Advanced LIGO laser. This strategy is similar to that used with Nd:YAG rods with undoped endcaps [21]. The solution presented in this thesis resolves the thermal lens through the thermal dependence of the index of refraction exclusively.

## CHAPTER 2 THEORY

### 2.1 Why Do Materials Absorb EM Energy?

When light strikes a medium, one of two outcomes are possible. The light can be scattered or absorbed. The case in which light scatters back towards the source is referred to as reflection. Similarly the case when light scatters into the medium is called transmission.

On a hot summer day, touch a windowpane. It feels warm if it has had sunlight falling upon it. This seems a rather trivial fact, until one asks why this pane of glass should be warmed by the sun. Afterall, the window is clear; in order to heat up, the pane needs to absorb light. Yet, apparently it transmits almost all sunlight perfectly and we can see the outside environment without loss of resolution.

This question can be answered by using the Maxwell's equations and a little approximation to the behavior of charges in a solid. Let us begin by considering a non-metallic media first as it applies to this thesis. Once again the Maxwell equations in a material are

$$\vec{\nabla} \times \vec{E} = -\frac{\partial \vec{B}}{\partial t}, \quad (2.1)$$

$$\vec{\nabla} \times \vec{H} = \frac{\partial \vec{D}}{\partial t} + \vec{J}, \quad (2.2)$$

$$\vec{\nabla} \cdot \vec{D} = \rho, \quad (2.3)$$

$$\vec{\nabla} \cdot \vec{B} = 0, \quad (2.4)$$

$$\vec{B} = \mu_0 (\vec{H} + \vec{M}), \quad (2.5)$$

$$\vec{D} = \epsilon_0 \vec{E} + \vec{P}, \quad (2.6)$$

where  $\vec{P}$  is polarization and  $\vec{M}$  is magnetization,  $\vec{B}$  is the magnetic field flux density,  $\vec{D}$  is the electric displacement.

Polarization is defined as the electric dipole moment per unit volume. More simply it is the intramaterial field induced when an external electric field is imposed on a dielectric substance

$$\vec{P} = \chi \epsilon_0 \vec{E}. \quad (2.7)$$

$\chi$  is the susceptibility and when multiplied by the permittivity of free space,  $\epsilon_0$ , gives the difference between a dielectric's permittivity and that of vacuum. It can be written as

$$\chi = \frac{\epsilon}{\epsilon_0} - 1. \quad (2.8)$$

Magnetization in non-conductive media is not a great factor so the magnetic field is  $\vec{B} = \mu_0 \vec{H}$ . Charges are restricted in movement; we can set  $\vec{\nabla} \cdot \vec{D} = 0$  since our non-conductors are electrically neutral. Therefore, we shall not carry it into the following analysis. We begin with the dynamic equation for the electric field,

$$\nabla \times \vec{E} = -\mu_0 \frac{\partial \vec{H}}{\partial t}. \quad (2.9)$$

We take the curl of the above equation,

$$\begin{aligned} \vec{\nabla} \times (\vec{\nabla} \times \vec{E}) &= -\mu_0 \vec{\nabla} \times \frac{\partial \vec{H}}{\partial t}, \\ \vec{\nabla} \times (\vec{\nabla} \times \vec{E}) &= -\mu_0 \frac{\partial}{\partial t} \vec{\nabla} \times \vec{H}. \end{aligned} \quad (2.10)$$

Substituting  $\nabla \times \vec{H}$  into the above equation we obtain

$$\nabla \times (\nabla \times \vec{E}) = -\mu_0 \frac{\partial}{\partial t} \left( \epsilon_0 \frac{\partial \vec{E}}{\partial t} + \frac{\partial \vec{P}}{\partial t} + \vec{J} \right). \quad (2.11)$$

Sending through the  $\frac{\partial}{\partial t}$  and replacing  $\epsilon_0 \mu_0$  with  $c^{-2}$ , we get

$$\vec{\nabla}(\vec{\nabla} \cdot \vec{E}) - \nabla^2 \vec{E} = -\frac{1}{c^2} \frac{\partial^2 \vec{E}}{\partial t^2} - \mu_0 \frac{\partial^2 \vec{P}}{\partial t^2} - \mu_0 \frac{\partial \vec{J}}{\partial t}. \quad (2.12)$$

If we move the  $\vec{E}$ -field terms to one side, the left-hand side becomes the familiar wave equation. The right-hand side contains source terms

$$\vec{\nabla}(\vec{\nabla} \cdot \vec{E}) - \nabla^2 \vec{E} + \frac{1}{c^2} \frac{\partial^2 \vec{E}}{\partial t^2} = -\mu_0 \frac{\partial^2 \vec{P}}{\partial t^2} - \mu_0 \frac{\partial \vec{J}}{\partial t}. \quad (2.13)$$

Why are we interested in terms on the right? The polarization term accounts for indices of refraction, birefringence, modulation, and a few other physical nuances. The single time derivative on current density accounts for a metal's ability to absorb energy from light fields that attempt to scatter through it. Since we shall not be considering the case of metallic free charges or currents traversing our non-conductor, we assign  $\vec{J} = 0$  and  $\vec{\nabla} \cdot \vec{E} = 0$ .

We assume in our model that the electric field modulates harmonically and is not so strong as to cause non-linear effects in the media. The weak field case allows us to model the response of the outer electrons by Hooke's law,  $\vec{F} = \kappa \vec{r}$ . Writing down a well known second order differential equation with linear damping we have

$$m \frac{d^2 \vec{r}}{dt^2} + m\gamma \frac{d\vec{r}}{dt} + \kappa \vec{r} = -e\vec{E}. \quad (2.14)$$

Here  $\kappa$  is our Hooke's constant.  $\gamma$  refers to the dampening coefficient for bound oscillating charges. As usual we assume that  $\vec{E}$  and  $\vec{r}$  are harmonic,

$$\vec{r} = \vec{r}_0 e^{-i\omega t}, \quad \vec{E} = \vec{E}_0 e^{-i\omega t}.$$

This gives us

$$-m\omega^2\vec{r}_0e^{-i\omega t} - im\gamma\omega\vec{r}_0e^{-i\omega t} + \kappa\vec{r}_0e^{-i\omega t} = -e\vec{E}_0e^{-i\omega t}. \quad (2.15)$$

Solving for  $\vec{r}_0$  gives us

$$\vec{r}_0 = \frac{-e\vec{E}_0}{-m\omega^2 + \kappa - im\omega\gamma}. \quad (2.16)$$

When we factor out the  $m$  we can rename  $\kappa/m$  as  $\omega_0^2$ . This is the effective resonance for the bound electron states [22],

$$\vec{r}_0 = \frac{\frac{-e\vec{E}_0}{m}}{\omega_0^2 - \omega^2 - i\omega\gamma}. \quad (2.17)$$

Now recall that polarization is  $\vec{P} = \vec{P}_0e^{-i\omega t} = -Ne\vec{r}$ . We substitute this into the equation for polarization and get

$$\vec{P} = \frac{\frac{-Ne^2\vec{E}}{m}}{\omega_0^2 - \omega^2 - i\omega\gamma}. \quad (2.18)$$

This equation always remains less than  $\infty$ , but, at  $\omega = \omega_0$ , polarization becomes purely imaginary. The consequences of this will become apparent momentarily.

Replace the polarization term in the wave equation and regroup the derivatives,

$$\begin{aligned} \nabla^2\vec{E} &= \left( \mu_0\epsilon_0 + \frac{\mu_0Ne^2}{m} \frac{1}{\omega_0^2 - \omega - i\omega\gamma} \right) \frac{\partial^2\vec{E}}{\partial t^2}, \\ &= \mu_0\epsilon_0 \left( 1 + \frac{Ne^2}{\epsilon_0m} \frac{1}{\omega_0^2 - \omega^2 - i\omega\gamma} \right) \frac{\partial^2\vec{E}}{\partial t^2}, \\ &= \frac{1}{c^2} \left( 1 + \frac{Ne^2}{\epsilon_0m} \frac{1}{\omega_0^2 - \omega^2 - i\omega\gamma} \right) \frac{\partial^2\vec{E}}{\partial t^2}. \end{aligned} \quad (2.19)$$

This differential equation is solvable through the separation of variables,

$$\vec{E}(\vec{r}, t) = \vec{R}(\vec{r})T(t), \quad (2.20)$$

$$\nabla^2\vec{R} = -K^2\vec{R}, \quad (2.21)$$

$$\frac{-1}{c^2} \frac{\partial^2 T}{\partial t^2} = K^2 T. \quad (2.22)$$

The solution of this is

$$\vec{E} = \vec{E}_0 e^{-i(\vec{K} \cdot \vec{r} - \omega t)} \quad (2.23)$$

where

$$K^2 = \frac{\omega^2}{c^2} \left( 1 + \frac{Ne^2}{\epsilon_0 m} \frac{1}{\omega_0^2 - \omega^2 - i\omega\gamma} \right). \quad (2.24)$$

The plane wave solution is one of only two popular solutions that can be quickly obtained. For the moment, we shall stick to the plane wave solution for this discussion. Focusing on the separation constant, we rewrite it more clearly,

$$K = k' + ik'', \quad (2.25)$$

where  $k'' = \alpha/2$ . We see that this is little more than a complex wavenumber.

What does this mean in terms of the electromagnetic wave? The exponential now possesses a decaying quality  $e^{-\alpha r}$  that is being multiplied times the free-space term,  $e^{-i\vec{k} \cdot \vec{r}}$ . Upon defining the intensity,  $I = |\vec{E}|^2$ ,  $\alpha$  gains a special name, the absorption coefficient [22]. This will be seen later in the model and experiment. Multiply by  $\omega/c$ ,  $K$  becomes the complex index of refraction,

$$N = \frac{\omega}{c} K. \quad (2.26)$$

As before we can separate this value into it's real and imaginary part,

$$N = n + i\mathcal{K}. \quad (2.27)$$

Just as before the existence of the imaginary index implies lossy media [22].

## 2.2 Birefringence: Innate and Thermal

We have now seen how to characterize and model the absorption of EM-waves in lossy media. This simple evaluation gives us an insight into how materials heat up when irradiated. The right hand portion of equation (2.13) also indicated that

electrically neutral materials can interact with electromagnetic fields. In a moment we shall see how dielectrics can alter electromagnetic waves through birefringence and multiple indices of refraction. These phenomena too can be affected by thermalization of host media. In order to understand how heating can generate “spatially induced birefringence,” a short adventure into native birefringence is required.

This jaunt starts with a redeclaration of the susceptibility. In real materials, it is a  $3 \times 3$  tensor, not a simple scalar [22]. Why has physics built a model like this? Simply because on the microscopic scale, the crystal’s charge distribution is not spherically symmetric. Rather, it follows “flow” paths imposed by the lattice that the nuclei support. Therefore, crystals with non-symmetric potentials will display multiple susceptibilities. This also points to anisotropies in phase velocities as will be seen. Incidentally, the only two lattice structures that yield isotropic susceptibility (and polarization) are cubic and trigonal [22, 23]. Crystals like sodium chloride, fluorite, and even diamond are isotropic. Should one not wish to work with a crystal, then glasses, gels, and fluids possess random structure that exhibits optical isotropy.

$$\vec{P} = \chi\epsilon_0\vec{E} \tag{2.28}$$

This implies that a modification to the displacement field may be made via

$$\begin{aligned} \vec{D} &= \epsilon\vec{E}, \\ \epsilon &\Rightarrow \epsilon_{mn} = \epsilon_0(1 + \chi_{mn}). \end{aligned} \tag{2.29}$$

The new permittivity’s modifier in parenthesis will become a bit more transparent later. Now, we write the Maxwell wave equation (again),

$$\nabla \times \left( \nabla \times \vec{E} \right) + \frac{1}{c^2} \frac{\partial^2 \vec{E}}{\partial t^2} = -\frac{1}{c^2} \chi_{mn} \frac{\partial^2 E}{\partial t^2}. \tag{2.30}$$

In Fourier space, this transforms into

$$\begin{aligned} \vec{k} \times (\vec{k} \times \vec{E}) + \frac{\omega^2}{c^2} \vec{E} &= -\frac{\omega^2}{c^2} \chi_{mn} \vec{E} \\ \hookrightarrow \vec{k}(\vec{k} \cdot \vec{E}) - k^2 \vec{E} + \frac{\omega^2}{c^2} \vec{E} &= -\frac{\omega^2}{c^2} \chi_{mn} \vec{E}. \end{aligned} \quad (2.31)$$

If we assume that  $\chi_{mn}$  is diagonal, we can expand this easily. The three equations for components along the  $x$ -,  $y$ -, and  $z$ -axes,

$$x : \left( -k_y^2 - k_z^2 + \frac{\omega^2}{c^2} \right) E_x + k_x k_y E_y + k_x k_z E_z = -\frac{\omega^2}{c^2} \chi_{11} E_x, \quad (2.32)$$

$$y : \left( -k_x^2 - k_z^2 + \frac{\omega^2}{c^2} \right) E_y + k_x k_y E_x + k_x k_z E_z = -\frac{\omega^2}{c^2} \chi_{22} E_y, \quad (2.33)$$

$$z : \left( -k_x^2 - k_y^2 + \frac{\omega^2}{c^2} \right) E_z + k_x k_y E_x + k_x k_z E_y = -\frac{\omega^2}{c^2} \chi_{33} E_z. \quad (2.34)$$

So we have an array of equations. An arbitrary yet contrived selection in propagation is now made. We set the wave vector,  $\vec{k}$ , along the  $x$ -axis,

$$k_x \neq 0, \quad k_y = k_z = 0, \quad E_x = 0. \quad (2.35)$$

Note that  $E_x = 0$  because  $E$ -fields are perpendicular to the wave vector. In turn, the above array yields

$$x : 0 = 0, \quad (2.36)$$

$$y : \left( -k_x^2 + \frac{\omega^2}{c^2} \right) E_y = -\frac{\omega^2}{c^2} \chi_{22} E_y, \quad (2.37)$$

$$z : \left( -k_x^2 + \frac{\omega^2}{c^2} \right) E_z = -\frac{\omega^2}{c^2} \chi_{33} E_z. \quad (2.38)$$

These two equations leave us with two phase velocities and two indices of refraction in the  $y$  and  $z$  direction,

$$k_y^2 - \frac{\omega^2}{c^2} = \frac{\omega^2}{c^2} \chi_{22} \quad (2.39)$$

$$\hookrightarrow k_y = \frac{\omega}{c} \sqrt{1 + \chi_{22}}, \quad (2.40)$$

$$k_z^2 - \frac{\omega^2}{c^2} = \frac{\omega^2}{c^2} \chi_{33} \quad (2.41)$$

$$\hookrightarrow k_z = \frac{\omega}{c} \sqrt{1 + \chi_{33}}. \quad (2.42)$$

The square root is the index of refraction for the  $y$ - and  $z$ -axes [22]. The  $x$ -axis' index of refraction can be obtained by inputting the  $\chi_{mn}$  appropriate for the  $x$ -axis,  $\chi_{11}$ . Although these susceptibilities appear to be material parameters, we will see that they have a dependence on temperature that effects birefringence.

### 2.3 Magneto-Optics and the Faraday Effect

In the previous section, the author mentioned “optically active” media. Optically active media entails any media that can adversely effect light as it passes through the material. “Adverse” effects include the rotation of the plane of polarization, phase modulation, and large scale frequency shifting (such as frequency doubling). The generation of such phenomena sometimes requires a static or dynamic electromagnetic field. In the case of frequency doubling, there is no need for extra external fields. For the application of Faraday rotators, magneto-optic activity is of importance.

An isotropic substance will not affect propagating light waves with the exception of increasing the optical path length.<sup>a</sup> As discussed before, this means simple cubic lattice crystals and glasses. However, when the dielectric is immersed

---

<sup>a</sup> Birefringence can be induced in isotropic materials through localized stress gradients. In this text we are concerned with thermally induced stress.

in a magnetic field, it becomes optically active. This effect was first encountered by Michael Faraday in 1845; therefore, magneto-optic rotators are referred to as Faraday rotators [22].

One's first impulse to explain the rotation of polarization, the Faraday effect, is to include the full Lorentz force in the damped differential equation seen in section (2.1),

$$m \frac{d^2 \vec{r}}{dt^2} + m\gamma \frac{d\vec{r}}{dt} + \kappa \vec{r} = -e\vec{E} - e\vec{v} \times \vec{B}_0, \quad (2.43)$$

$$\vec{v} = \frac{d\vec{r}}{dt}, \quad (2.44)$$

where  $\vec{B}_0$  is the external magnetic field flux density [22]. Again, we assume that the electric field and position vector are harmonic,

$$-m\omega^2 \vec{r} - im\omega\gamma \vec{r} + \kappa \vec{r} = -e\vec{E} + i\omega \vec{r} \times \vec{B}_0. \quad (2.45)$$

Next  $-Ne$  is multiplied through to convert position vectors into polarization vectors,

$$-Ne(-m\omega^2 \vec{r} - im\omega\gamma \vec{r} + \kappa \vec{r}) = -Ne(-e\vec{E} + i\omega \vec{r} \times \vec{B}_0), \quad (2.46)$$

$$\hookrightarrow (-m\omega^2 - im\omega\gamma + \kappa) \vec{P} = Ne^2 \vec{E} + i\omega \vec{P} \times \vec{B}_0. \quad (2.47)$$

This expands to...

$$(-m\omega^2 - im\omega\gamma + \kappa) \begin{pmatrix} P_x \\ P_y \\ P_z \end{pmatrix} = Ne^2 \begin{pmatrix} E_x \\ E_y \\ E_z \end{pmatrix} + i\omega \begin{pmatrix} (P_y B_{0z} - P_z B_{0y}) \\ (P_z B_{0x} - P_x B_{0z}) \\ (P_x B_{0y} - P_y B_{0x}) \end{pmatrix}. \quad (2.48)$$

Choosing the magnetic field to be in the  $z$  direction simplifies the problem and somewhat simulates what a magneto-optically active crystal sees in a Faraday

rotator,

$$(-m\omega^2 - im\omega\gamma + \kappa) \begin{pmatrix} P_x \\ P_y \\ P_z \end{pmatrix} = Ne^2 \begin{pmatrix} E_x \\ E_y \\ E_z \end{pmatrix} + ie\omega \begin{pmatrix} P_y B_{0z} \\ -P_x B_{0z} \\ 0 \end{pmatrix}. \quad (2.49)$$

Solving for  $P_x$ ,  $P_y$ , and  $P_z$ , we get a set of complex solutions,

$$P_x = \frac{Ne^2(-iB_z E_y e + E_x m(i\gamma + \omega))}{(B_z^2 e^2 + m^2(\gamma - i\omega)^2)\omega}, \quad (2.50)$$

$$P_y = \frac{Ne^2(iB_z E_y e + E_x m(i\gamma + \omega))}{(B_z^2 e^2 + m^2(\gamma - i\omega)^2)\omega}, \quad (2.51)$$

$$P_z = \frac{E_z Ne^2}{-im\gamma\omega - m\omega^2}. \quad (2.52)$$

In their full form (dampening included) one can see that after collecting electric field terms that the susceptibility matrix does not have a real diagonal. This is completely due to the dampening introduced. However, this is a rather difficult expression to utilize. If we disregard dampening, complex components can be packed into the susceptibility's off diagonal terms. This leads into a rather useful phenomenon as we shall see.

$$\vec{P} = \chi_{mn}\epsilon_0\vec{E} \quad (2.53)$$

$$\chi_{mn} = \begin{pmatrix} \chi_{11} & \chi_{12} & 0 \\ -\chi_{12} & \chi_{22} & 0 \\ 0 & 0 & \chi_{33} \end{pmatrix} \quad (2.54)$$

where  $\chi_{12}$  is imaginary.

Without dampening, the components are as follows:

$$\chi_{11} = \frac{Ne^2}{m\epsilon_0} \left[ \frac{\omega_0^2 - \omega^2}{(\omega_0^2 - \omega^2) - \omega^2\omega_c^2} \right], \quad (2.55)$$

$$\chi_{33} = \frac{Ne^2}{m\epsilon_0} \left[ \frac{1}{(\omega_0^2 - \omega^2)} \right], \quad (2.56)$$

$$\chi_{12} = \frac{iNe^2}{m\epsilon_0} \left[ \frac{\omega\omega_c}{(\omega_0^2 - \omega^2) - \omega^2\omega_c^2} \right], \quad (2.57)$$

Here  $\omega_c = \frac{eB}{m}$  and  $\omega_0 = \sqrt{\frac{k}{m}}$  [22].

As with section (1),  $\chi_{mn}$  and it's multipliers  $\epsilon_0$  and  $\vec{E}$  becomes the righthand side of the inhomogeneous wave equation.

$$\vec{k} \times (\vec{k} \times \vec{E}) = \frac{-\omega^2}{c^2} (1 + \chi_{mn}) \vec{E} \quad (2.58)$$

A pair of wave numbers are produced this time. However, unlike section 1, these wave numbers differ for the two circular polarizations—left and right.

$$k = \frac{\omega}{c} \sqrt{1 + \chi_{11} \pm \Im(\chi_{12})} \quad (2.59)$$

The two indices of refraction that come from this are,

$$n_{right} = \sqrt{1 + \chi_{11} + \Im(\chi_{12})} \quad (2.60)$$

$$n_{left} = \sqrt{1 + \chi_{11} - \Im(\chi_{12})} \quad (2.61)$$

We can find the specific rotary power for a polarized light wave by first starting with circularly polarized light,

$$\vec{U} = \frac{1}{2} \begin{pmatrix} 1 \\ i \end{pmatrix} e^{ik_R z} + \frac{1}{2} \begin{pmatrix} 1 \\ -i \end{pmatrix} e^{ik_L z}. \quad (2.62)$$

where  $U$  is a normalized field vector and  $k_L$  and  $k_R$  are the wave vectors for left and right circularly polarized light respectively [22, 14]. Continuing we obtain

$$\begin{aligned}
\vec{U} &= \frac{1}{2} \begin{pmatrix} e^{ik_R z} + e^{ik_L z} \\ i(e^{ik_R z} - e^{ik_L z}) \end{pmatrix}, \\
&= \frac{1}{2} e^{\frac{i}{2}(k_R+k_L)z} \begin{pmatrix} e^{\frac{i}{2}(k_R-k_L)z} + e^{-\frac{i}{2}(k_R-k_L)z} \\ i(e^{\frac{i}{2}(k_R-k_L)z} - e^{-\frac{i}{2}(k_R-k_L)z}) \end{pmatrix}, \\
&= e^{\frac{i}{2}(k_R+k_L)z} \begin{pmatrix} \cos \frac{1}{2}(k_R - k_L)z \\ \sin \frac{1}{2}(k_R - k_L)z \end{pmatrix}. \tag{2.63}
\end{aligned}$$

Since  $k = \frac{2\pi}{\lambda} = \frac{\omega}{c}$ , we see that this gives us specific rotary power,

$$\delta = (n_{right} - n_{left}) \frac{\pi}{\lambda}. \tag{2.64}$$

Finally, multiplying through crystal length,  $l$ , reveals the angle by which the plane of polarization is **rotated**,

$$\beta = (n_{right} - n_{left}) \frac{\pi l}{\lambda}. \tag{2.65}$$

This can be written as a function of magnetic field,

$$\beta = V B_z l. \tag{2.66}$$

where  $V$  is the Verdet constant,  $B_z$  is the magnetic field in the direction of propagation, and  $l$  again is the length of the media [14].

One will notice that the rotation angle does not depend on propagation direction with respect to the magnetic field. This is why optically active media can be exploited for use in Faraday isolators.

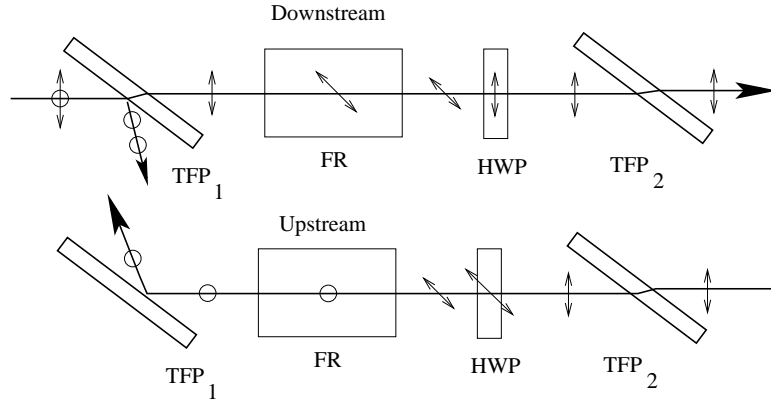


Figure 2–1: A schematic describing the operation of a Faraday isolator. TFP = thin film polarizer; FR = Faraday rotator; HWP = half-wave plate. The direction of light propagation is indicated by the large arrow head. Additional arrows indicate the angle of light polarization with respect to the optical axis. Circles indicate light with polarization vectors perpendicular to the page. Arrows at 45° indicate light whose polarization has been rotated by 45° with respect preceding polarization angle. Vertical arrows describe polarization vectors that lie in the page. All polarization vectors in this schematic are perpendicular to the optical axis.

## 2.4 Faraday Isolator

Physically, a Faraday isolator is a simple apparatus that serves the same purpose as an electrical diode<sup>b</sup> for optical systems. The layout shown in Figure 2.1 consists of two polarizers, the Faraday rotator,<sup>c</sup> and a half-wave plate.

The first polarizer, “TFP 1,” selects the polarization of light to be passed. Light polarized perpendicularly to the polarizer reflects off “TFP 1” and out of the beamline.<sup>d</sup> The light that reaches the Faraday rotator has its polarization altered by angle  $\beta$ , as stated in the preceding discussion. Typically this angle is

<sup>b</sup> A device based on a pn-junction that ideally permits current to flow in one direction only.

<sup>c</sup> A magneto-optically active medium surrounded by a strong magnet encased in an optical housing.

<sup>d</sup> “Beamline” refers to the primary or intended path of the laser light.

45°. The half-wave plate then rotates the light back to its original polarization thereby allowing the second polarizer, “TFP 2”, to transmit the laser downstream.

Upstream propagating light initially observes the second polarizer. Supposing the light passes into the Faraday isolator, it meets the half-wave plate which imparts a 45° rotation on the electric field. Next the Faraday rotator completes the polarization’s angular displacement by another 45°. The upstream propagating light is now reflected out of the beamline by “TFP 1.” The Jones matrices for the separate components are as follows:

- Polarizer

$$M_{polarizer} = \begin{pmatrix} 1 & 0 \\ 0 & 0 \end{pmatrix}; \quad (2.67)$$

- Faraday rotator

$$M_{FR} = \begin{pmatrix} \cos\beta & -\sin\beta \\ \sin\beta & \cos\beta \end{pmatrix}; \quad (2.68)$$

- Half wave plate

$$M_{HWP} = \begin{pmatrix} \cos 2\alpha & \sin 2\alpha \\ \sin 2\alpha & -\cos 2\alpha \end{pmatrix}; \quad (2.69)$$

where  $\beta$  equals  $\pi/4$  and  $\alpha$  equals  $\pi/8$  [14].

Multiplying the components in the downstream propagating solution we get

$$M_{FI} = \frac{1}{\sqrt{2}} \begin{pmatrix} \cos\beta + \sin\beta & 0 \\ \cos\beta - \sin\beta & 0 \end{pmatrix}. \quad (2.70)$$

For any fields propagating upstream, the solution becomes

$$M_{FI} = \frac{1}{\sqrt{2}} \begin{pmatrix} \cos\beta - \sin\beta & 0 \\ \cos\beta + \sin\beta & 0 \end{pmatrix}. \quad (2.71)$$

Notice that these calculations do not include the final polarizer observed by the beam. By setting  $\beta$  to  $45^\circ$ , we see that the matrices are orthogonal. This represents the isolator's diode-like behavior. Therefore, placing an isolator between two optical components in series will decouple the upstream component from the downstream component.

## 2.5 Thermal Lens

The preceding sections have introduced how seemingly transparent materials can absorb light energy and heat up. The author assumed that the medium was being irradiated evenly via plane waves; furthermore, the author assumed that none of the material's optical parameters were thermally dependent (i.e.,  $\chi \neq \chi(\mathbf{T})$ ). If we allow the medium's parameters to be thermally dependent, we find that the optical path length through the medium changes in three manners [15]. Explicitly, they are written out as

$$\Delta OPL = \Delta OPL_{innate} + \Delta OPL_{thermal} + \Delta OPL_{stress} + \Delta OPL_{expansion}. \quad (2.72)$$

The initial term,  $\Delta OPL_{innate} = n_0 L$ , refers to the increase in optical path length as a medium is placed into a beamline. The term  $n_0$  is the material's index of refraction at a constant temperature [22, 15].

Second in line stands the thermal response of the index of refraction. When we let  $\chi_{mn}$  be thermally dependent, this implies that the index of refraction varies with respect to temperature,

$$\Delta OPL_{thermal}(\vec{r}) = \frac{dn}{dT} L \Delta T(\vec{r}), \quad (2.73)$$

where  $dn/dT$  is the derivative of refractive index with respect to temperature and  $\Delta T(\vec{r})$  is the difference in temperature between  $r = 0$  and a radial point,  $r$ , [15, 21].

The third component of the equation is the stress term. Its approximation is

$$\Delta OPL_{stress}(\vec{r}) = \frac{-n_0^3}{2} \rho_{12} \alpha L \Delta T(\vec{r}). \quad (2.74)$$

Here  $\rho_{12}$  is the photo-elastic coefficient, and  $\alpha$  is the thermal expansion coefficient.

This effect hails from the elasto-optic effect

$$\Delta\left(\frac{1}{n^2_i}\right) \approx \sum_{j=1}^6 p_{ij} S_{ij} + \sum_{j=1}^3 r_{ij} E_{ij}. \quad (2.75)$$

The change in the inverse square index of refraction is directly proportional to the photo-optic coefficient,  $p_{ij}$ , the strain tensor,  $S_{ij}$ , radial direction,  $r_{ij}$ , and electric field,  $E_{ij}$ . A spatial deformation in a piezo crystal generates a voltage by changing charge distributions within the crystal [15].

Equally, an oscillating electric field or acoustic wave will cause changes in the index of refraction through charge coupling. However, since the frequency of light tends to be greater than the charge response time, the photo-elastic term is not usually included in the *OPL* calculation [24].

Fourth in this list is expansion. Possibly the best known of the  $\Delta OPL$  terms, this term tracks surface deformation due to local temperature differences and total on-axis length increase.

$$\Delta OPL_{expansion} \approx 2\alpha n w \Delta T(\vec{r}) \quad (2.76)$$

where  $\alpha$  is the coefficient of thermal expansion,  $n$  is the index of refraction, and  $w$  is the Gaussian-beam waist size in the medium. We can neglect bulk expansion due to the boundary conditions imposed on the medium sitting in the beamline. If the optic is far larger than the beam's diameter, we can assume that the colder region clamps the expansion of the heated region. Thus, expansion in directions transverse to the beam will be held to a minimum. Expansion only occurs at the end faces of the media [15, 16, 17, 18, 19, 25]. According to Strain *et al* [17] we can

approximate the expansion of the surface—also called the change in sagitta—by assuming that the volume entertaining expansion extends a waist length into the material. Therefore, the above equation is sound in its approximation.

One will note that each of the three terms contains a single power of the temperature difference. This temperature difference can be calculated using assumptions made in the  $\Delta OPL_{expansion}$  term plus a set of implicit assumptions [15]. Stated again for clarity they are

- the medium does not excessively attenuate the beam;
- the dimensions of the optical medium far exceeds that of the laser’s Gaussian waist;
- heat flow is exclusively radial;
- the absorption throughout the media is uniform.

We first begin with the heat diffusion equation.

$$\nabla^2 T + \frac{q}{k_{th}} = \frac{1}{D_{th}} \frac{\partial T}{\partial t} \quad (2.77)$$

where  $T$  is temperature,  $q$  is the heat source distribution ( $\text{Wm}^{-2}$ ),  $k_{th}$  is the thermal conductivity ( $\text{Wm}^{-1}\text{K}^{-1}$ ), and  $D_{th}$  is the thermal diffusivity ( $\text{m}^2\text{s}^{-1}$ ). Since we are not interested in transient solutions, the right hand side equals zero<sup>e</sup>.

$$\nabla^2 T + \frac{q}{k_{th}} = 0 \quad (2.78)$$

Since LIGO depends on the  $TEM_{00}$  mode, we shall use this as our heat source,  $q(r)$ .

$$q(r) = \frac{2\alpha P}{\pi w_0^2} e^{-\frac{2r^2}{w_0^2}} \quad (2.79)$$

---

<sup>e</sup> Hello and Vinet studied transients for large mirrors to be used in gravitational wave detectors [19].

We can now continue.

$$\begin{aligned} \frac{1}{r} \frac{d}{dr} r \frac{d}{dr} T &= -\frac{1}{k_{th}} \left( \frac{2\alpha P}{\pi w_0^2} e^{-\frac{2r^2}{w_0^2}} \right) \\ r \frac{dT}{dr} &= -\frac{2\alpha P}{\pi k_{th} w_0^2} \int r e^{-\frac{2r^2}{w_0^2}} dr \end{aligned} \quad (2.80)$$

Rewriting the exponent as a sum we get...

$$\begin{aligned} r \frac{dT}{dr} &= -\frac{2\alpha P}{\pi k_{th} w_0^2} \int r \sum_{n=0}^{\infty} (-1)^n \frac{\left(\frac{2r^2}{w_0^2}\right)^n}{n!} dr, \\ T(r) &= -\frac{2\alpha P}{\pi k_{th} w_0^2} \sum_{n=0}^{\infty} \frac{(-1)^n \left(\frac{2}{w_0^2}\right)^n}{2(n+1)n!} \int (r^2)^n \frac{d(r^2)}{2} + A \ln(r) + B, \\ T(r) &= \frac{\alpha P}{4\pi k_{th}} \sum_{n=0}^{\infty} \frac{(-1)^{n+1} \left(\frac{2}{w_0^2}\right)^{n+1}}{(n+1)^2 n!} (r^2)^{n+1} + A \ln(r) + B. \end{aligned}$$

If we change the summation by setting  $j = n + 1$  this solution becomes...

$$\begin{aligned} T(r) &= \frac{\alpha P}{4\pi k_{th}} \sum_{j=1}^{\infty} \frac{(-1)^j \left(\frac{2r^2}{w_0^2}\right)^j}{j j!} + A \ln(r) + B, \\ A &= 0, \\ B &= T_0. \end{aligned}$$

The first coefficient was set to zero to prevent the equation from diverging as  $r \rightarrow \infty$ , and  $B$ 's value is then obtained by setting  $r = 0$  [17]. The final result for the temperature difference profile is

$$\Delta T(r) = \frac{\alpha P}{4\pi k_{th}} \sum_{j=1}^{\infty} \frac{(-1)^j \left(\frac{2r^2}{w_0^2}\right)^j}{j j!}. \quad (2.81)$$

Let's evaluate this expression. We observe that the function is zero at  $r = 0$ . As we plot the profile we see for several waist lengths the temperature difference falls as expected. However, the exponent on  $r$  causes the function to go to positive or negative infinity depending on whether the  $j$  factor is even or odd, respectively. Since the laser effectively does not exist outside 3 waist lengths, the laser never

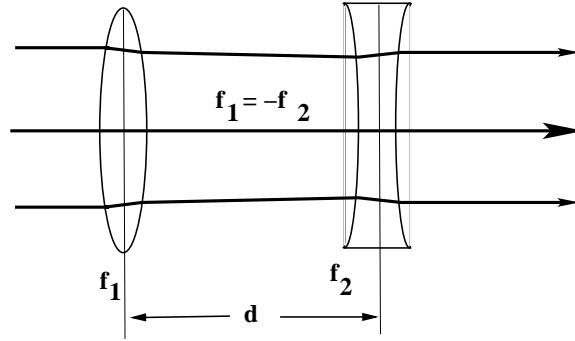


Figure 2–2: The toy model visualized.  $f_1 =$  positive lens focal length;  $f_2 =$  negative lens focal length;  $d =$  separation distance. A positive thin lens can be compensated by a negative thin lens. Should the focal lengths,  $f_1, f_2$  of the two lenses greatly exceed the separation distance,  $d$ , the effect of the first lens can be negated by the second lens if the magnitude of the two focal lengths are equal.

observes this part of the model [17]. Therefore, within physical beam dimensions this model of temperature difference is valid.

Homogeneous heating does not result in a lens being generated; it only yields an increased *OPL*. This is why a temperature gradient is necessary. Its existence causes phase differences in the EM wave.

This rather innocuous looking solution permits us to proceed with the development of an analysis scheme to simulate the thermal lens and its compensation.

## 2.6 Toy Model and Practice

We have now introduced the concept of thermal lensing as it applies to flat face media. A lens of any sort simply alters the phase of the imposed field. This results in the field intensifying at the focus of the “lens.” A physical lens imposes the same type of phase distortions. However the phase difference enters through the differences in physical path length of the media. Taking this into account, we can develop a toy model of the requirements for the eventual solution. The focal length of a two lens telescope is

$$\frac{1}{f_{tot}} = \frac{1}{f_1} + \frac{1}{f_2} - \frac{d}{f_1 f_2}, \quad (2.82)$$

where  $d$  is the distance between the two lenses. Assuming that the two lenses' focal lengths exceed  $d$ ,  $d \ll f_1, f_2$ , we can simplify this the lensmaker's equation to the form

$$\frac{1}{f_{tot}} = \frac{1}{f_1} + \frac{1}{f_2}. \quad (2.83)$$

Effectively this happens in the real world because the focal length change in a low-absorbing media is small. Nevertheless, let  $f_1$  be a positive lens of strength “ $f$ .” It is simple to see that a negative lens of equal strength will be required to set  $f_{tot} = \infty$ . This is equivalent to stating that no lenses are in the beamline.

However, compensation of a thermal lens is not as simple as indicated by the above equations. The lensmaker's equations are built around spherical non-deformable lenses. Thermal lenses are not spherical nor are they unchanging. We can take advantage of  $\Delta OPL$  through the  $\Delta OPL_{thermal}$  [20]. Strictly writing the  $dn/dT$  lensing terms for two materials yields

$$\Delta OPL = \frac{dn_1}{dT} L_1 \Delta T_1(r) + \frac{dn_2}{dT} L_2 \Delta T_2(r). \quad (2.84)$$

We see that when  $\Delta OPL$  is set to zero, the two  $OPL$  terms have opposite signs,

$$\frac{dn_1}{dT} L_1 \Delta T_1(r) = -\frac{dn_2}{dT} L_2 \Delta T_2(r). \quad (2.85)$$

We can factor out the power in the thermal difference terms since the target medium and its compensator material will observe nearly the same laser intensity,

$$\frac{dn_1}{dT} L_1 \frac{\alpha_1}{k_{th1}} = -\frac{dn_2}{dT} L_2 \frac{\alpha_2}{k_{th2}}. \quad (2.86)$$

Since lengths, thermal conductivity, and absorption coefficient are always positive, the  $dn/dT$  of the compensator material must be opposite that of the target material.

Although a compensation material may have an appropriate  $dn/dT$ , a parameter must be available to properly compensate the thermal lens in the first medium. Length of the medium 1,  $dn_1/dT$ ,  $dn_2/dT$ , and thermal profile are fixed for both materials. Only length of the second (compensation) medium remains as a variable in repairing thermal lenses.

One should also note that this linearized model implies that an optimum length of compensation material exists for each thermally lensing material. Further contemplation indicates that the compensation strategy is independent of incident power. The latter conclusion should not be accepted as truth. This model is based on a linear expansion of thermally induced effects in materials and does not consider the possibility of nonlinear effects such as melting, frequency conversion, or other effects that occur beyond the envelope of assumptions. This does not make the model incorrect as a first approximation to correction of thermal lenses [20].

### 2.7 Wavefront Model

Solutions that track the paraxial wave profile require numerical solutions. Since we are only interested in axial motions of the beam and not pointing deflections, we can restrict the propagation to the Laguerre-Gauss mode representation<sup>f</sup> [15, 17, 20]. We begin the algorithm by declaring the  $TEM_{00}$  mode's field,

$$u_{00} = \sqrt{\frac{2}{\pi w_0^2}} e^{-\frac{r^2}{w_0^2}}. \quad (2.87)$$

To match the toy model's thin lens type assumptions, we place this field in the center of the first crystal, TGG. The thermal lens' phase shift is then applied,

$$u_{aber} = u_{00} e^{i \frac{2\pi \Delta OPL_{TGG}}{\lambda}}. \quad (2.88)$$

---

<sup>f</sup> See section 1, chapter 3

$\lambda$  is the laser wavelength in a vacuum. The aberrated beam is written in the Laguerre-Gauss basis,

$$u_{aber} = \sum_{n=0}^{\infty} c_{n0} L_{n0} \left( \frac{2r^2}{w_0^2} \right) u_{00}. \quad (2.89)$$

Using Laguerre-Gauss overlap integrals, we can obtain the coefficients,

$$c_{n0,uncomp} = 2\pi \int_0^{\infty} u_{aber}^* u_{n0} r dr. \quad (2.90)$$

We next propagate the wavefront to the position of the compensator material, FK51 Schott glass. This is performed by applying the Gouy phase shift. The Gouy phase denotes how the wavefront's shape changes as it propagates through free space. It acquires its phase from the ratio of propagated distance versus half the collimation length. Implemented the new field becomes

$$u'_{aber} = \sum_{n=0}^{\infty} c_{n0} L_{n0} \left( \frac{2r^2}{w_0^2} \right) u_{00} e^{i2\pi\Phi_{Gouy}}. \quad (2.91)$$

Explicitly  $\Phi_{Gouy} = \arctan\left(\frac{z}{Z_R}\right)$ .  $Z_R$  is half the collimation distance, the Rayleigh range,

$$Z_R = \frac{\pi w_0^2}{\lambda}. \quad (2.92)$$

At the center of the glass, the counter-thermal lens is applied,

$$u_{comp} = u'_{aber} e^{\frac{i2\pi\Delta OPL_{FK51}}{\lambda}}. \quad (2.93)$$

Notice the  $\Delta OPL$  is negative in this case and will subtract from the original thermally induced phase shift. Again, we expand this field in the local Laguerre-Gauss basis,

$$u_{comp} = \sum_{n=0}^{\infty} c_{n0} L_{n0} \left( \frac{2r^2}{w_0^2} \right) u_{00}. \quad (2.94)$$

The amplitudes once again are found through overlap integrals,

$$c_{n0,comp} = 2\pi \int_0^\infty u_{comp}^* u_{n0} r dr. \quad (2.95)$$

We now have the amplitudes of the modes that compose the two uncompensated and compensated laser fields. Since we are interested in the power retention of the  $TEM_{00}$  mode, we need only find the magnitude squared of the first Laguerre-Gauss coefficient. The resulting intensities are normalized to one at zero incident power,

$$I_{00,uncomp} = |c_{00,uncomp}|^2, \quad (2.96)$$

$$I_{00,comp} = |c_{00,comp}|^2. \quad (2.97)$$

Notice that the representation in each basis calls for an infinite sum. We must be careful here during the construction of the model and use enough of the basis to regenerate the smooth transitions that a real wavefront would observe. This lack of precision encouraged the use of twenty Laguerre-Gauss modes to represent the infinite sum.

We need a third solution to compare the strategy of thermal compensation against focus compensation. Focus compensation uses the tactic of finding an optimum spherical lens to refocus the fundamental mode. A solution can be found by searching for a fundamental Gaussian mode that generates the largest overlap integral.

$$I_{opt} = \left| 2\pi \int_0^\infty u_{aber}^* v_{opt} r dr \right|^2 \quad (2.98)$$

The constants used in this analysis are in Table 2.1

Table 2-1: A table of material constants.

Material	$\alpha(\text{cm}^{-1})$	$k_{th}(\text{WmK}^{-1})$	$dn/dT (10^{-6}\text{K}^{-1})$	$L(\text{mm})$
TGG	$6.3 \times 10^{-3}$	7.4	20	35
FK51	$9.2 \times 10^{-3}$	0.9	-6	67

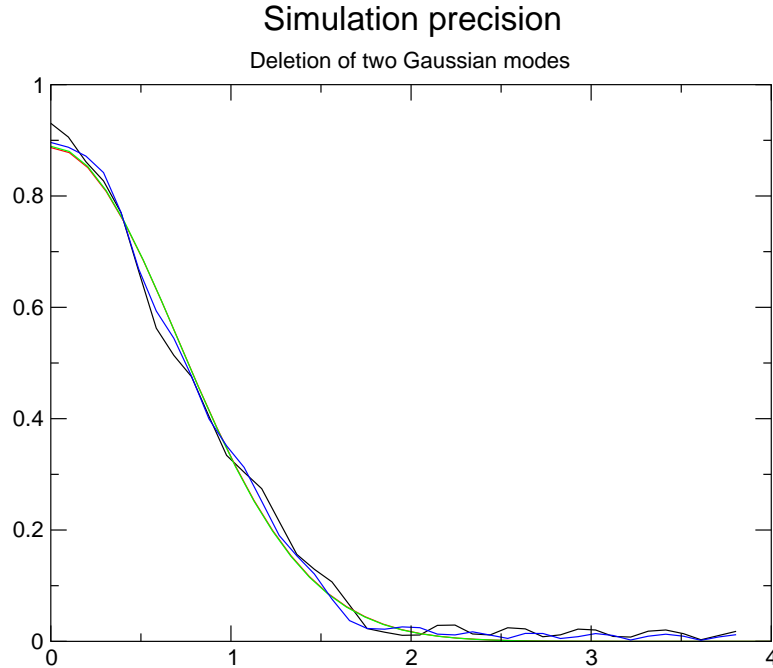


Figure 2–3: This is a demonstration of simulation precision. The green line shows plots a Gaussian curve based on the analytical solution. The blue curve approximates the Gaussian curve using nineteen Hermite-Gauss modes. The black curve approximates the Gaussian with only eighteen Hermite-Gauss modes. Notice the over estimation and artifactual ripples in the approximations especially in the wings.

One should note that the absorption coefficient for TGG was measured in-house. The FK51’s  $\alpha$  term was fitted following data acquisition. Schott’s internal transmittance report for FK51 gave a standardized term of  $8 \times 10^{-3} \text{cm}^{-1}$ . Thermal conductivity was obtained for TGG from Mansell et al. [15] and for FK51 from Schott’s data sheet<sup>g</sup> [26]. The absorption coefficient will become especially important in chapter 3’s analysis section.

The results of these intensity terms are plotted below with respect to incident power. The rapidly falling curve is the uncompensated  $TEM_{00}$  mode. Without

---

<sup>g</sup> Schott Glass data sheet 487845.

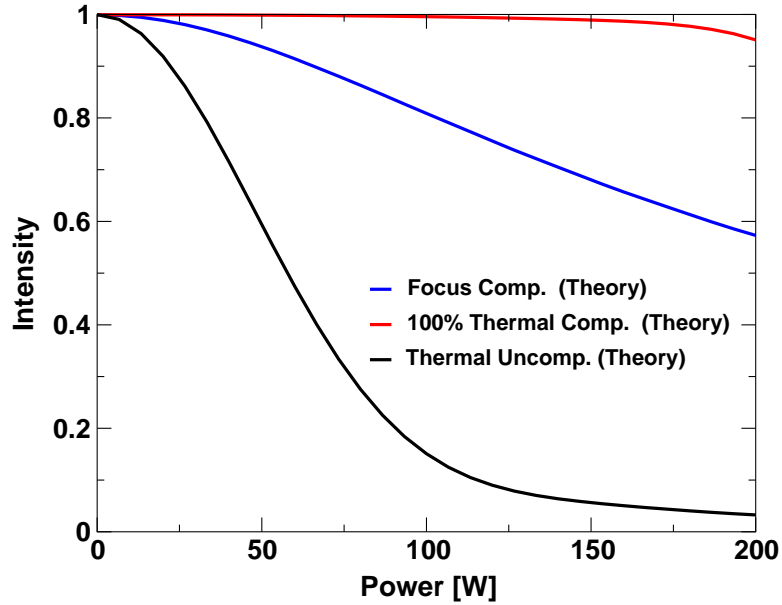


Figure 2–4: A plot of simulated normalized intensity remaining in the  $TEM_{00}$  mode versus incident laser power. The uncompensated, black, curve drops rapidly due to the thermal lens shifting laser light from the fundamental spatial mode into higher order  $TEM$  modes. The focal compensation curve is generated by determining the best fixed lens basis on the radius of curvature of the wavefront in the spherical approximation for each power. The red curve represents ideal thermal compensation. At 180 W, the retained intensity in the  $TEM_{00}$  mode drops to 95 percent. The rolls off is due to the separation between the lensing and compensating materials in the beamline.

compensation, the amount of power in the  $TEM_{00}$  mode drops to 5 percent at 180 W. Focus compensation appears to retain 60 percent of the original modal power. This still does not meet Advanced LIGO requirements of greater than 95 percent power retention. An ideal compensator, however, would keep 97.5 percent light power in the fundamental mode at 180 W. At 200 W, the ideal compensator drops to 94.5 percent. Unlike the previous section’s toy model, the separation distance between the two materials cannot be ignored. The Gouy phase shift removes the possibility of perfect compensation.

## CHAPTER 3 EXPERIMENT AND ANALYSIS

The following chapter discusses the experiment in detail. This chapter concerns itself with the methods and techniques used in observing thermal lenses. We begin with a section regarding the detectors and design of the tabletop. Following this will be a briefing of the equipment and any peculiarities found. Then, comes a subsequent description of the experimental setup. Next, measurement methods of optical absorption coefficients will ensue. A description of procedures, data collection, and analysis will conclude this chapter.

### 3.1 Design

In chapter two, we learned that thermal lenses can alter the spatial mode structure of a laser. In order to observe how much light is moved from the fundamental  $TEM_{00}$  mode to higher order modes, one needs an instrument to separate the different spatial modes. This device is a simple non-degenerate scanning Fabry-Perot cavity. All other optical components found on the table are based around redirecting, mode matching, or thermalizing materials that interact with light entering the cavity.

Also, the use of a Fabry-Perot cavity flows logically from the design of the large gravitational wave detectors. Since all optical gravity wave detectors utilize Fabry-Perot interferometers whose working point is the  $TEM_{00}$  mode, a scheme that incorporates a cavity would offer insight into how badly thermal lenses depreciate signal contrast and how well compensation recovers this signal contrast.

## 3.2 How to Analyze a Thermal Lens

### 3.2.1 Scanning Fabry-Perot Cavity

The scanning non-degenerate Fabry-Perot cavity forms the heart of this experiment's detection scheme. So we shall spend a little time in the theory of its characteristics and operation. The Fabry-Perot cavity is a physically simple device. It consists of two facing mirrors. These mirrors are aligned in the beamline in order to temporarily trap light passing through them. This results in light waves bouncing off the mirrors multiple times. Numerous contained counter-propagating waves generate interference. Therefore, the Fabry-Perot cavity can be referred to as an interferometer or an optical resonator <sup>a</sup> [14, 22, 27].

To understand the nature of the cavity we investigate how fields act within the cavity. The analysis starts by writing down the Collins integral [14],

$$E_2(x_2, y_2) = -\frac{i\pi}{\lambda B} e^{-i\omega t} \iint E_1(x_1, y_1) e^{\frac{i\pi}{\lambda B} (Ax_1^2 + Dx_2^2 - 2x_1x_2 + Ay_1^2 + Dy_2^2 - 2y_1y_2)} dx_1 dy_1. \quad (3.1)$$

This equation is generalized Kirchhoff integral written in terms of the  $ABCD$  matrix<sup>b</sup> used in ray and wave optics. Here  $\lambda$  is the wavelength of the light field, and  $\omega$  is the angular frequency of the light field. The subscripts 1 and 2 denote two different analysis planes perpendicular to the  $z$  or optical axis. One should note that this equation assumes the light beam is cylindrically symmetric.

A solution that retains the field distribution yet allows the beam's amplitude and beam diameter change as the beam propagates through an optical system is a

---

<sup>a</sup> The term resonator will be used interchangeably with Fabry-Perot cavity.

<sup>b</sup> see Appendix A

beam with a Gaussian field distribution,

$$E_1(x_1, y_1) = E_0 e^{-\frac{x_1^2 + y_1^2}{w_0^2}}, \quad (3.2)$$

where  $w$  is the laser beam's diameter. This type of beam can also be written in the following form,

$$E_1(x_1, y_1) = E_0 e^{-\frac{ik}{2q_1}(x_1^2 + y_1^2)}. \quad (3.3)$$

$q$  is a wavefront's complex radius of curvature,<sup>c</sup> and  $k$  is the wavenumber.

Within a resonator, a wavefront regenerates itself upon each round trip—amplitude and lateral extent included. This stipulation requires an eigensolution of the Collins integral be found,

$$\gamma E_1(x_2, y_2) = -\frac{ie^{ikL}}{2Lg_2\lambda_0} \iint E_1(x_1, y_1) e^{\frac{i\pi}{2Lg_2\lambda_0}(G(x_1^2 + y_1^2 + x_2^2 + y_2^2) - 2(x_1x_2 - y_1y_2))} dx_1 dy_1. \quad (3.4)$$

The round trip ray transfer matrix,

$$M = \begin{pmatrix} G & 2Lg_2 \\ \frac{G^2 - 1}{2Lg_2} & G \end{pmatrix}, \quad (3.5)$$

has been applied to the integral thereby simulating the periodicity of the optics.

The term  $g_j$  equals

$$1 - \frac{L}{\rho_j} \quad (3.6)$$

where  $L$  is the optical path length of the cavity, and  $\rho_j$  is the radius of curvature of the  $j^{\text{th}}$  mirror.  $G$  is  $2g_1g_2 - 1$ .  $\gamma$ , the eigenvalue in the Collins equation takes note of any diffractive losses (scattering, absorption by cavity medium).

---

<sup>c</sup> see Appendix A

Implementing the Gaussian field a family of solutions to the cavity field may be found. Expressed in cylindrical and rectangular coordinates, the fields on mirror  $j$  are as follows [14]:

- Circular symmetry, Laguerre-Gauss modes ( $TEM_{pl}$ )

$$E_{pl}^j(r, \Phi) = E_0 \left[ \frac{\sqrt{2}r}{w_j} \right]^l L_{pl} \left( \frac{2r^2}{w_j^2} \right) e^{-\frac{r^2}{w_j^2}} \begin{pmatrix} \cos(l\Phi) \\ \sin(l\Phi) \end{pmatrix} \quad (3.7)$$

$$\gamma = \exp \left[ ik \left( 2L - \frac{\lambda}{\pi} (2p + l + 1) \arccos \sqrt{g_1 g_2} \right) \right] \quad (3.8)$$

- Rectangular symmetry, Hermite-Gauss modes ( $TEM_{mn}$ )

$$E_{pl}^j(x, y) = E_0 e^{-\frac{x^2+y^2}{w_j^2}} H_m \left( \frac{\sqrt{2}x}{w_j} \right) H_n \left( \frac{\sqrt{2}y}{w_j} \right) \quad (3.9)$$

$$\gamma = \exp \left[ ik \left( 2L - \frac{\lambda}{\pi} (m + n + 1) \arccos \sqrt{g_1 g_2} \right) \right]. \quad (3.10)$$

Conditions for resonance demands  $\gamma$  is real. However, setting  $\gamma = 1$  the effort of finding the resonance frequencies is simplified,

$$\begin{aligned} \gamma &= e^{ik \left( 2L - \frac{\lambda}{\pi} (2p+l+1) \arccos \sqrt{g_1 g_2} \right)} \\ 1.0 &= e^{ik \left( 2L - \frac{\lambda}{\pi} (2p+l+1) \arccos \sqrt{g_1 g_2} \right)}. \end{aligned}$$

Resonance frequencies may now be found by utilizing  $\gamma$ 's exponent.

$$\begin{aligned} \rightarrow 0 &= \left( 2L - \frac{\lambda}{\pi} (2p + l + 1) \arccos \sqrt{g_1 g_2} \right) \\ 2L &= \frac{\lambda}{\pi} (2p + l + 1) \arccos \sqrt{g_1 g_2} \\ \frac{1}{\lambda} &= \frac{1}{2L\pi} (2p + l + 1) \arccos \sqrt{g_1 g_2} \\ \frac{c}{\lambda} &= \frac{c}{2L\pi} (2p + l + 1) \arccos \sqrt{g_1 g_2} \\ \nu_{pl} &= \frac{c}{2L\pi} (2p + l + 1) \arccos \sqrt{g_1 g_2}. \end{aligned}$$

These are the frequencies for the transverse modes [14, 22, 27]. Axial modes can be added by superposition to obtain the final result,

$$\nu_{pl\tilde{q}} = \frac{c}{2L} \left( \tilde{q} + \frac{2p+l+1}{\pi} \arccos \sqrt{g_1 g_2} \right). \quad (3.11)$$

An identical treatment applies to Hermite-Gauss modes,

$$\nu_{mn\tilde{q}} = \frac{c}{2L} \left( \tilde{q} + \frac{m+n+1}{\pi} \arccos \sqrt{g_1 g_2} \right). \quad (3.12)$$

Let us look carefully at these results. If we set each  $g = 0$  through  $\rho = L$ , we find that the resonant frequencies are all spaced  $\frac{c}{4L}$  apart. Also, laser frequencies that exhibit higher order spatial modes resonate simultaneously with fundamental resonance modes. Optical resonators with these characteristics are called “confocal” cavities [14]. These are not applicable to this experiment.

If we construct a cavity with  $g_1 g_2$  between 0 and 1, we see that the no two spatial modes resonate at the same frequency unless their indices yield coincidence. For example the Hermite-Gauss  $TEM_{11}$ <sup>d</sup> and the Laguerre-Gauss  $TEM_{10}$ <sup>e</sup> modes share the same frequency. Such cavities are nondegenerate and can be used to sift through various optical modes. This is the type of cavity necessary for successfully analyzing modal content of laser radiation.

In order to observe the separate spatial modes of the laser radiation entering the cavity, we must change the length of the cavity. Although there lies the possibility of altering the radius of curvature of the end mirrors or changing the axial frequency of the laser, these are both less practical methods of moving the Fabry-Perot through the free spectral range. A brief discussion of the free spectral range will follow. Changing the length of the cavity will change the cavity’s

---

<sup>d</sup> The  $TEM_{11}$  mode is often called the “cloverleaf” mode.

<sup>e</sup> Referred to as the “bull’s eye” mode.

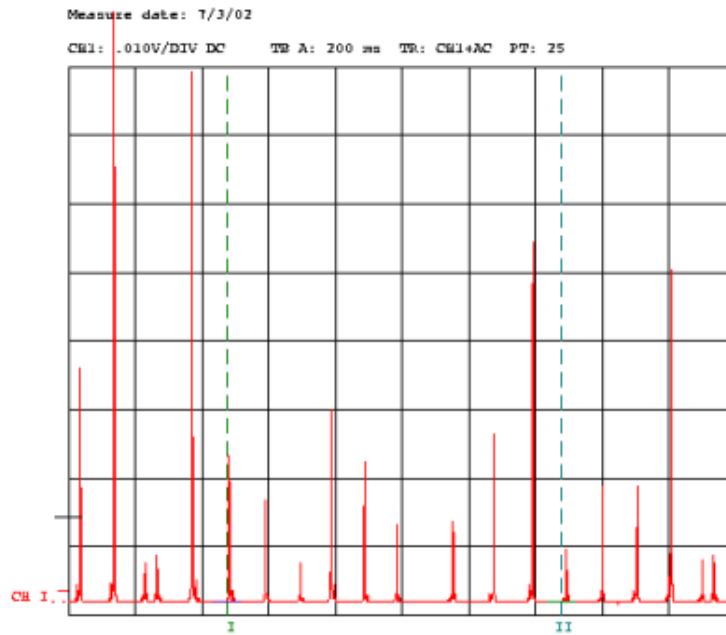
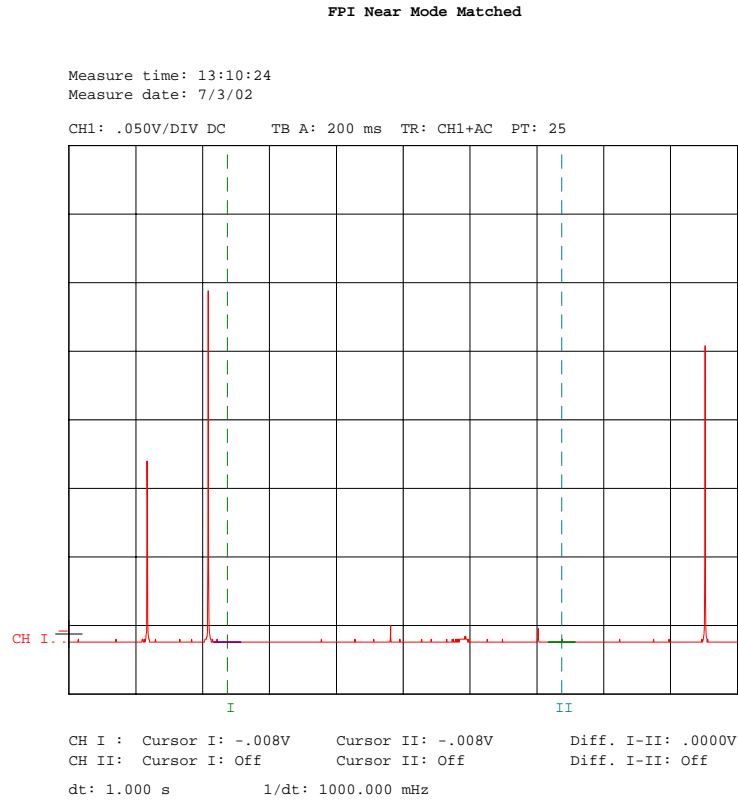


Figure 3–1: A graphic of this experiment’s Fabry-Perot transmission curves over the full free spectral range. The data displays DC voltage versus time. Implicit on the horizontal axis is mirror position. The two largest peaks are the fundamental resonances,  $TEM_{00}$ . The second highest peak is the Laguerre-Gauss  $TEM_{10}$  “bull’s eye” mode followed by the Hermite-Gauss  $TEM_{10}$  tilt mode. One can see the number of modes passing through is limited to several higher order modes. One should also notice the ability of this nondegenerate cavity to separate the probe laser’s spatial modes.

resonance frequency. In this experiment, a piezoelectric crystal altered the length of the cavity by approximately 1 micrometer.

A few other characteristics of Fabry-Perot cavities are worth mentioning since they affect experimental results. These are free spectral range, bandwidth, finesse, and maximum circulating power [14, 27]. Most of these attributes, based on mirror reflectivity, determine cavity quality.



Notes:

Figure 3–2: A transmission curve showing the cavity nearly aligned. This figure spans the free spectral range of the cavity. Notice the suppression of higher order modes. The tallest three peaks are the  $TEM_{00}$  mode in intensity. The next highest peaks are the Hermite-Gauss  $TEM_{10}$  tilt mode in transmission. Height discrepancies are due to the cavity not full achieving resonance.

Free spectral range (abbreviated FSR) is defined by

$$FSR = \frac{c}{2L}. \quad (3.13)$$

This number informs one how far apart two resonances of the same spatial frequency sit from one another in frequency space [14, 22]. For example, if one had a 1 meter long cavity on  $TEM_{00}$  resonance, one would have to slew through nearly 150 MHz of frequency space before the  $TEM_{00}$  was observed again.

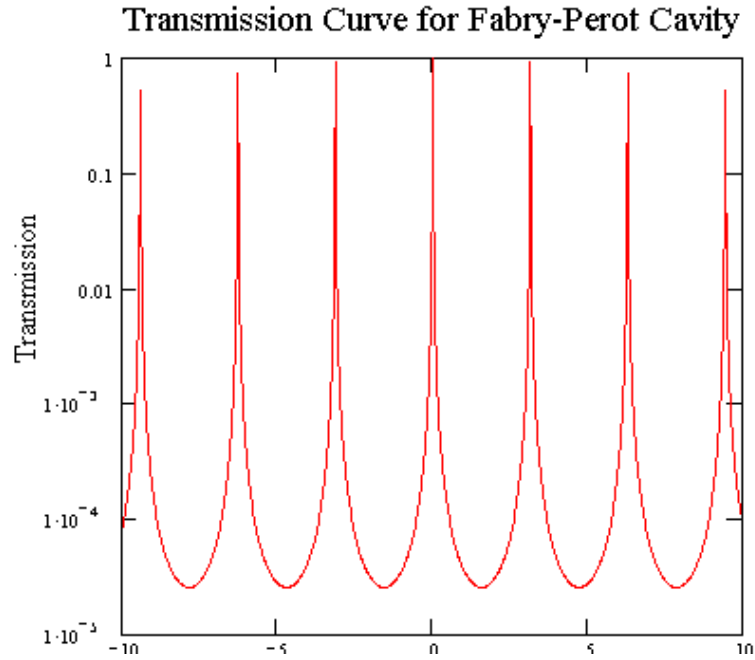


Figure 3–3: This transmission curve is calculated for the Fabry-Perot cavity on fundamental resonance. Normalized intensity is plotted versus phase number.  $k = 2\pi/\lambda$ ;  $L =$  mirror separation length. This indicates in order to sweep through the free spectral range, one must either alter the input laser wavelength or change the mirror separation length. Peak fall off is due to computer precision. All peak maxima achieve 100 percent transmission on resonance.

The bandwidth or full width at half maximum of the transmission peaks is given by the equations,

$$\delta\nu = \left| \ln(|\gamma|^2 \sqrt{R_1 R_2}) \right| \frac{c}{2\pi L}. \quad (3.14)$$

Here  $R_j$  is the amplitude reflectivity of the  $j^{\text{th}}$  mirror modulus squared. One empirical method of determining the bandwidth is to scan the frequency of the light entering a fixed length Fabry-Perot. A plot of transmission intensity versus frequency can be created. A cavity sitting on resonance will transmit any light wave whose frequency falls within the bandwidth.

Most resonant electronic circuits have a measure of quality [14, 27]. Resonators are no different. The quality factor's expression is not altered by the idea

that light waves possess frequencies of hundreds of terahertz ( $10^{14}$  Hz),

$$\begin{aligned} Q &= 2\pi(FSR)\tau, \\ &= \frac{\nu}{\delta\nu}. \end{aligned} \tag{3.15}$$

The  $\tau$  in the first equation is the decay time for circulating energy in a cavity to fall by a factor of  $e^{-1}$  [14],

$$\begin{aligned} \tau &= \frac{L}{c} \frac{1}{|\ln(|\gamma|^2\sqrt{R_1R_2})|}, \\ &= \frac{1}{2\pi\delta\nu}. \end{aligned} \tag{3.16}$$

$\nu$  in the second equation is the frequency at which  $Q$  is being analyzed. A second, more often quoted equation is finesse [14, 27],

$$\begin{aligned} F &= \frac{FSR}{\delta\nu}, \\ &= \frac{\pi}{|\ln(|\gamma|^2\sqrt{R_1R_2})|}. \end{aligned} \tag{3.17}$$

Many books, such as Siegman [27] and Davis [24], also document finesse as

$$F = \frac{\pi\sqrt{r_1r_2}}{1 - r_1r_2}. \tag{3.18}$$

Both terms yield information regarding how long light will circulate within a cavity. Greater circulation times generate greater contrast between resonant and nonresonant cavity states. Also it is interesting to notice

$$\begin{aligned} Q &= 2\pi(FSR)\tau, \\ &= \frac{FSR}{\delta\nu}, \\ &= F. \end{aligned}$$

At their resonance frequencies, resonant electrical circuits store large quantities of energy and power. This too occurs with the Fabry-Perot cavity. Energy density

inside the cavity can be acquired via

$$\rho_{E,max} = \frac{I_0}{c} \frac{1 - R^2}{(1 - |\gamma|^2 \sqrt{R_1 R_2})^2}, \quad (3.19)$$

where  $I$  is the incident intensity[14]. Circulating power can be acquired from  $\rho$  by multiplying with lightspeed and cross-sectional area of the beam,

$$P_{max} = P_0 \frac{1 - R^2}{(1 - |\gamma|^2 \sqrt{R_1 R_2})^2}, \quad (3.20)$$

where  $P_0$  is the incident laser power. The amount of circulating optical power becomes important when trying to hold a Fabry-Perot cavity on resonance.

Although the input laser power can be negligible, circulating powers can result in physical expansion of resonator housing material.

The above equations for this experiment yield the following results:

The device itself is reflection coated for 1064 nm laser light. The operating wavelength for this cavity is 1064 nm. The “ $g$ ” product lies comfortably between 0 and 1. Reflectivities of approximately 0.99 percent deliver high finesse that resulted in large contrast. Calculating the difference between the “bull’s eye” mode and the  $TEM_{00}$  mode, we obtain 744 MHz. The free spectral range exceeds this value by 193 MHz. Therefore the two modes of interest should be clearly distinguishable from one another. This was confirmed during the data runs; the two modes well separated.

The single drawback of high finesse lay in the cavity’s ability to remain on resonance. Due to the large number of bounces observed within the cavity, power in the cavity increased by a factor of 199. This level of power provided a heat source that pushed the cavity off resonance. This problem was remedied by placing a second polarizing beamsplitter and halfwave plate immediately behind the interaction region to reduce the amount of cavity input light.

Table 3-1: Analyzer cavity characteristics

speed of light	
$c$	299792458 m s <sup>-1</sup>
Radii of curvature	
Mirror, M <sub>1</sub>	0.3 m
Mirror, M <sub>2</sub>	0.5 m
Cavity length	
$L$	0.16 m
$g$ -factors	
$g_1$	0.467
$g_2$	0.68
$g_1g_2$	0.3177
Free Spectral Range	
FSR	0.9369 GHz
Reflectivity	
Mirror, M <sub>1</sub>	0.99
Mirror, M <sub>2</sub>	0.99
Finesse	
$F$	313
Input laser power	
$P_0$	0.100 W
Circulating Power	
$P_{max}$	20.0 W
Eigenvalue	
$\gamma$	1

### 3.2.2 Beam Profiling

A second and less precise method of observing thermal lenses is beam profiling. This method involves acquiring cross-sections of the laser at multiple distances. A  $\chi^2$  fit is then performed to determine the laser waist size and position as incident power on target is varied. The  $\chi^2$  fit is based on the waist propagation equation,  $w(z)$  found from the complex-q,<sup>f</sup>

$$q_0 = \frac{i\pi w_0^2}{\lambda},$$

$$q(z) = z + q_0,$$

$$\frac{1}{q(z)} = \frac{1}{z + \frac{i\pi w_0^2}{\lambda}},$$

$$\frac{1}{q(z)} = \frac{z}{z^2 + \frac{\pi^2 w_0^4}{\lambda^2}} - \frac{\frac{i\pi w_0^2}{\lambda}}{z^2 + \frac{\pi^2 w_0^4}{\lambda^2}},$$

$$Z_R = \frac{\pi w_0^2}{\lambda},$$

$$\frac{1}{q(z)} = \frac{1}{z + \frac{Z_R^2}{z}} - \frac{i\lambda}{\pi w_0^2 \left(1 + \left(\frac{z}{Z_R}\right)^2\right)},$$

$$\frac{1}{q(z)} = \frac{1}{R(z)} - \frac{i\lambda}{\pi w(z)^2},$$

$$\rightarrow w(z) = w_0 \sqrt{1 + \frac{z}{Z_R}}. \quad (3.21)$$

---

<sup>f</sup> The complex-q is a fundamental part of the eigensolution to the Fresnel-Kirchoff equation; see Appendix A.

$R(z)$  is the radius of curvature of the wave front. The term  $Z_R$  is the Rayleigh range. This is the half-distance that a wave front with infinite radius of curvature and a finite waist will remain “collimated” [27]. At the Rayleigh distance, the beam waist expands to a factor  $\sqrt{2}$  larger than the waist [14, 27].

Examining this equation we find that the waist equation is hyperbolic. Beyond the Rayleigh range the beam more closely follows the asymptotes. This implies that for accurate waist measurements one needs to obtain data outside the Rayleigh range. Obtaining data within the Rayleigh range often results in poor  $\chi^2$  fits. This often occurs when there exists a large beam waist. Large beam waists cause long collimation distances and therefore slow radii changes. When this is combined with errors of approximately ten percent,  $\chi^2$  analyses can result in poor fits or multiple fit solutions.

The beam profiler instrument functions by timing how long light falls on a pyroelectric detector as a slit rotates past. A computer program then interprets this time as beam width. Using a rapid response detector constructed for use in the near infrared, an intensity profile can be plotted. The detector used in this experiment was obtained from Photon-Inc. and will here on be referred to by its model name, “BeamScan.”

### 3.3 Layout of Table

#### 3.3.1 Table Overview

The overview of the table will give a structured look at the tabletop experiment’s components. We shall start with the two lasers followed by a note on all components. The probe beamline will then be discussed through the cavity and tandem photodetectors. The high power laser’s beamline will be explained before continuing into procedures.

### 3.3.2 Components

#### Lasers

For any probe laser to stably resonate in an Fabry-Perot analyzer cavity, the laser itself must be stable. The probe laser must not be powerful enough to induce a thermal lens in any of the media with which it interacts. The laser incorporated into this experiment was a LightWave Non-Planar Ring Oscillator (NPRO) model 126. This laser delivers 450mW of 1064 nm radiation from a neodymium doped yttrium aluminum garnet (Nd:YAG) monolithic crystal that is pumped by laser diodes. The NPRO was chosen for its stability and reliability. A turnkey device, this laser delivers 94.6 percent of its power in the  $TEM_{00}$  mode.<sup>g</sup>  $M^2$  for this laser was approximately 1.1. All other light fields lie in higher-order modes.

Heat for our optical crystal and glass comes from a neodymium doped yttrium lithium fluoride (Nd:YLF) crystal laser<sup>h</sup> built by Photon Industries, Inc. This laser delivered 52 Watts at 93.4 percent output capacity. Similar to the probe laser, this laser also had an  $M^2$  of 1.1 verifying a nearly pure  $TEM_{00}$  mode. Unlike the probe laser, Photon Industries utilized a linear resonator whose transverse modes were limited by a mechanical aperture. Although  $M^2$  measurements confirmed the linear resonator's transverse modes were restricted, the design still permitted the Nd:YLF to "mode hop." Resonators that "mode hop" have several axial frequencies that compete for energy simultaneously. Therefore these lasers exhibit frequency modulation. Modulation of the high power laser light was an advantage. Frequency instability prohibited much light from entering and passing through the analyzer cavity thereby protecting downstream sensors. Light that eventually seeped through increased the noise floor on the photodetectors.

---

<sup>g</sup>  $M^2$  measurements verified the NPRO's operational quality.

<sup>h</sup> This laser will be referred to as the pump or YLF after this point.

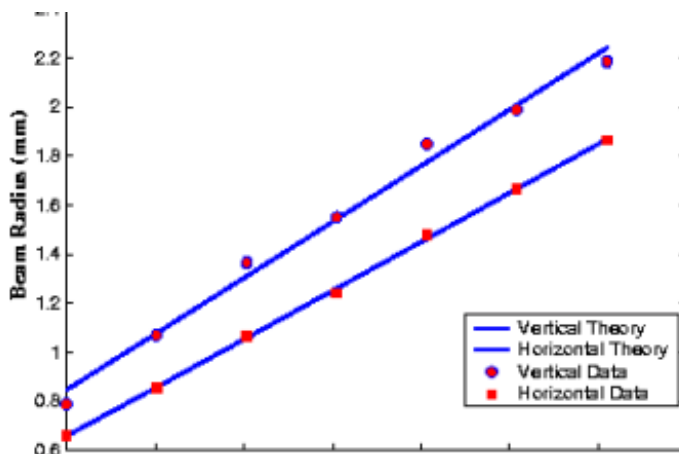


Figure 3-4: Graphed above are the  $\chi^2$  fits of the Nd:YAG NPRO laser's vertical and horizontal axes. The vertical axis radius exceeds the horizontal axis radius indicating a slight ellipticity. This is inherent in solid state lasers. Error bars are approximated by the datum size.

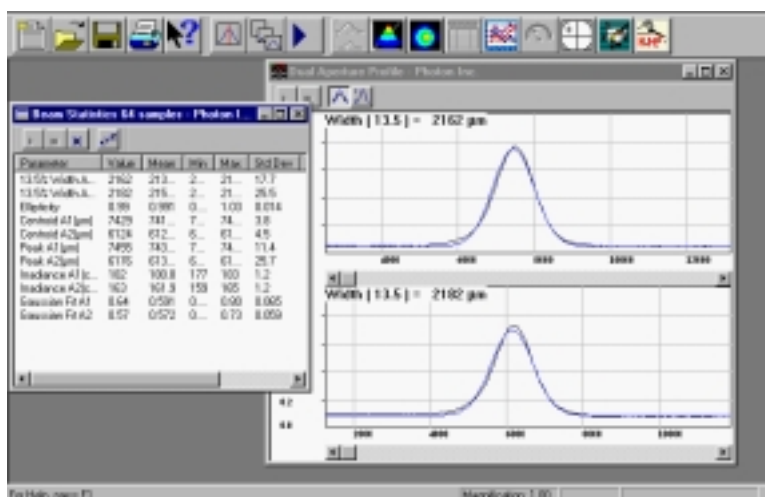


Figure 3-5: This screenshot of BeamScan's proprietary computer program illustrates the Gaussian nature of the pump laser used.

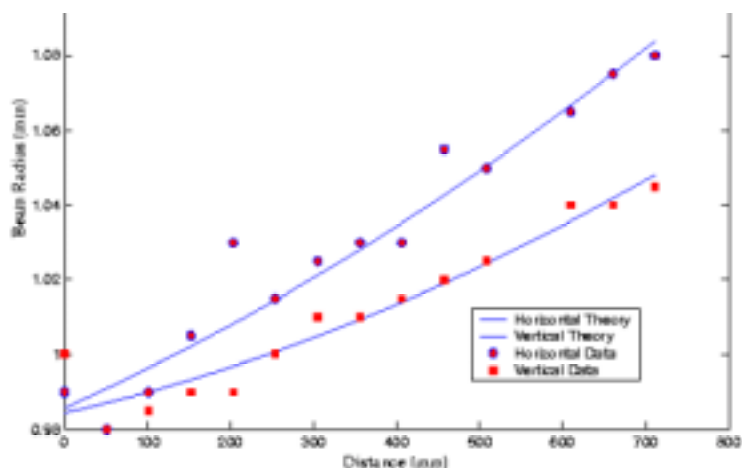


Figure 3–6: This figure is the  $\chi^2$  fit of the pump laser. Similar to the probe laser, this laser possesses a slight asymmetry. Data variation is due to the BeamScan experiencing difficulty when observing full laser power. Error bars are approximated by the datum size.

### Table

The experiment was assembled on a 4 ft.×8 ft.×1 ft. Newport Research Series Plus table. These tables are filled with silicon oil to aid in intra-table vibration dampening. The floor mounts were XL-A series. Isolation from vibration was not deemed critically important. The YLF laser’s water cooler/power supply transmitted some vibration through the water lines directly into the table. The top of the table had a breadboard configuration with bolt points spaced 1 in. on center. The boltholes accepted 0.25" × 20 bolts. The experiment often exploited the rectangular arrangement of the boltholes. This permitted a more precise method of obtaining beam profilometry.

### Test Optics

The centerpieces of this experiment were obtained from two manufacturers. A Faraday rotator was obtained from Litton AirTronics. The compensation material,

FK51 glass wedges, were supplied by Schott Glass company. The rotator was based on terbium gallium garnet crystal technology and housed in a neodymium based magnet housing. This magnet generates approximately 0.6 Tesla in its bore. The AirTronics rotator also had a large aperture, 1 cm in diameter. The TGG crystal's dimensions were 1 cm×3 cm. In order for the rotator to function properly, the crystal was required to be centered within the magnet.

Two FK51 Schott glass wedges were ordered with the dimensions 3.65 cm by 9.67 cm by 2.2 cm. Both wedges were anti-reflection coated for 1053 nm and 1064 nm. They were placed closely together to prevent multiple inter-wedge scattering.

#### Low Power Faraday Isolator

A Faraday isolator was used to retain the stability of the probe laser and to further protect the laser from any high power radiation that might propagate upstream. The Faraday isolator chosen for the probe laser was obtained from Electro-Optics Technology (EO-Tech). EO-Tech's isolator was based on terbium gallium garnet technology similar to the Faraday rotator used for the thermal compensation experiment.

#### Waveplates

All four waveplates were acquired from CVI Laser Corporation.<sup>i</sup> All three half-wave plates were based on air gap separated quartz plates. As quartz is already birefringent at room temperature, these crystals do not impose added polarizations. The short physical length of the wave plates also minimized the possibility of thermal lensing, especially important for pump laser power control. The fourth plate was a quarter-wave plate and was deployed only during overlap alignment.

---

<sup>i</sup> CVI serves as CVI Laser Corporation's unofficial abbreviation.

### Polarizers

Three polarizers were bought from CVI. Two rectangular thin film polarizers (TFPs) were used to create the test Faraday isolator and limit the region of pump laser interaction. These polarizers functioned on Brewster's angle ( $53^\circ$ ). They were designed for 30 dB suppression of "s" polarized light at high incident laser powers. BK7 glass formed the substrate and did not appear to develop a substantial thermal lens when tested using beam profilometry. The third polarizer was a polarizing beam splitter cube (PBSC). Its substrate was also BK7, and it also yielded a 30 dB extinction ratio. This particular type of beam splitter was not incorporated into the high power region since it displays poor thermal lens performance. The poor performance was caused by an overlap between incident and reflected radiation within the incident prism. This performance was observed in all PBSCs and was dimension independent. Therefore, the PBSC was used to enhance the extinction of any pump radiation that escaped towards the analyzer cavity.

The fourth polarizer was bought from New Focus. A Glan-Thompson 5525 calcite based polarizer provided 50 dB extinction. This polarizer was used with a CVI half-wave plate and CVI PBSC during absorption coefficient measurements for TGG and FK51 (see section 3.5). This polarizer was not intended to withstand a high power laser; it was never used in the thermal lensing setup.

### Mirrors

One-inch steering mirrors for this experiment came from two sources, New Focus and CVI. No mirror in this experiment except for the analyzer cavity was set for zero incidence. Nonetheless, New Focus mirrors were designed for zero incidence and included a silvered back decal to prevent light leakage. These mirrors comprised the pump laser's aiming periscopes. CVI mirrors designed for 100

percent reflection for s-polarized light <sup>j</sup> at 45 degrees incidence were used in the probe laser periscopes. Although these mirrors were designed to operate at two different incidence angles, we found the mirrors to be interchangeable.

Mirrors placed in the analyzer cavity were manufactured by REO. Indicated in the preceding section, both mirrors had reflectivities of approximately 0.99 for 1064 nm radiation. The input coupler and output coupler mirrors had radii of curvatures of 0.3 m and 0.5 m respectively. Unlike the steering mirrors, the cavity mirrors' diameters were 1 cm. The thickness of the mirrors was also 1 cm. REO formed the substrates from BK7 glass.

### Lenses

Newport fabricated lenses for mode matching telescopes 1, 2, and 3. A substrate of fused silica was coated with an anti-reflective coating for the one micron infrared regime. Fused silica possesses half the  $dn/dT$  of TGG. The short path length of the silica and preshaped curvature suppressed thermal lensing or induced birefringence.

### Cavity and Associated Electronics

The cavity itself was machined out of stainless steel. Steels such as Invar and crystals such as fused quartz display less susceptibility to thermal expansion. However, an analyzer cavity's performance does not rely on remaining on resonance. Rather, the device sweeps through the resonance state to obtain peak values. Therefore, this material was deemed suitable. Also, a screw end design allowed the input coupler mirror to be manually moved through 7 cm of travel. This permitted the cavity's eigenmodes to be altered should the experiment necessitate it. The

---

<sup>j</sup> Mirrors had high reflective coatings for 1064 nm light. The bandwidth included 1053 nm.

mirrors rested on end caps that were attached to the tube via three screws. Viton-O ring spacers between the end cap and the cavity tube permitted the mirrors to be aligned independently. Situated between the output coupler mirror and the end cap was a piezoelectric crystal tube (PZT). This crystal when stressed by  $\pm 200$  V moved the output coupler through approximately one micron, two free spectral ranges.

The piezocrystal driver was assembled in-house. The design for both the power supply and PZT driver come from Gerhard Heinzl at the Laser Zentrum in Hannover (LZH), Germany. The driver primary components consisted of two high voltage operational amplifiers, Apex's model OP-87. These op-amps received amplitude fluctuation signals from two smaller OP-27 op-amps. The latter devices relayed signal data from an external function generator that was set to a triangle waveform. A DC offset allowed for manual tuning of the output coupler position in the cavity. However, excessive heat in the OP-87s due to everyday operation and poor heat sink quality, resulted in the driver's voltage slowly wandering. The direction of voltage change was monotonic, predictable, and therefore did not influence the experiment.

A Thurlby Thandar Instruments, TTI, model TG120 function generator sent a 0.7 Hz triangle wave to the PZT driver. This function generator was chosen for its simplicity of operation. It also came with an output attenuator which when switched off increased the output amplitude by factor 10.

### Photodiodes

A ThorLabs Inc. PDA255 photodiode was chosen for this experiment. Powered by a AC/DC transformer-rectifier, this photodiode observed voltage into the  $10^2$  microvolt range. This design incorporated a BNC coaxial cable connector to

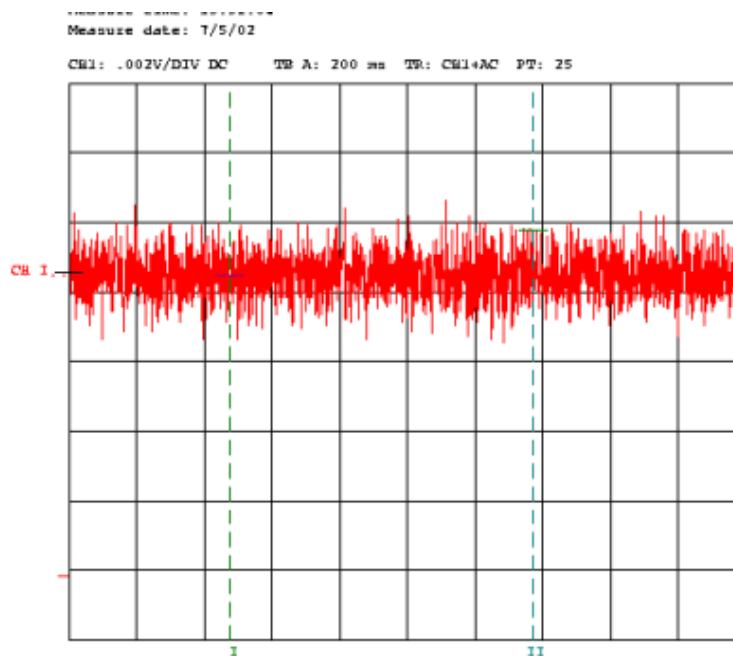


Figure 3–7: Oscilloscope voltage versus time data set showing the noise background for the PDA225. Note, no lasers were active during this data acquisition.

deliver current signals. The small diode (1 mm x 1 mm) was silicon based. Unfortunately the AC power source resulted in output signal fluctuations in the tens of microvolts.

A ThorLabs Inc. DET110 12 V battery powered fast response diode aided in absorption coefficient measurements. DC battery power provided a quieter baseline from which to operate. Linearity tests indicate that the device remained predictable from low incident light levels to near saturation.

In addition to the photodiodes, a dichromatic CCD and monitor were employed to observe modes resonating within the cavity. Tandy Corporation assembled the CCD and monitor. This strategy of utilizing a camera to see light in the cavity permitted for a faster alignment as well as immediate lower order mode recognition.

### Oscilloscope

A Digital Hameg Model 407 oscilloscope was chosen to capture the photodiode signal. Similar to many other digital oscilloscopes, the Hameg utilizes a

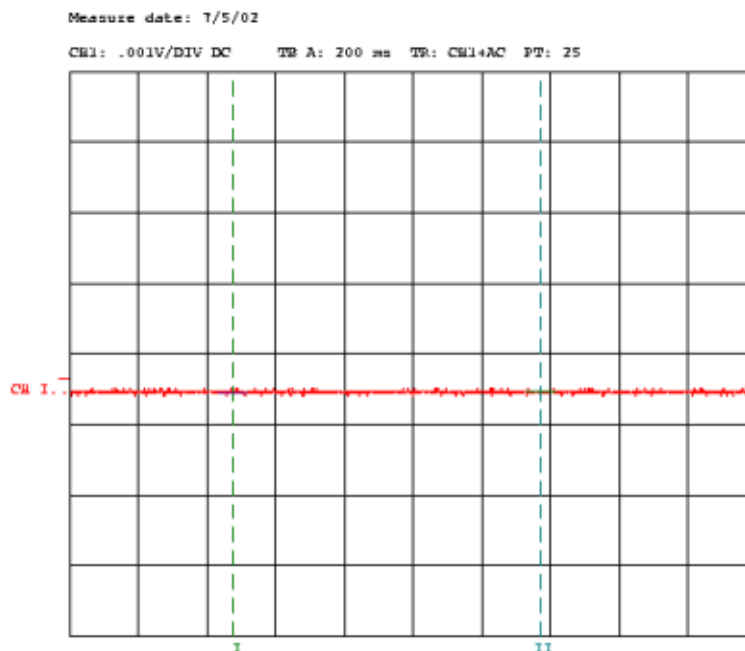


Figure 3–8: Oscilloscope data set showing the noise background for the DET110. Notice the reduction in background noise.

megaohm input impedance. ThorLabs designed their photodiode for a 50 Ohm output impedance. Therefore, a 50 Ohm terminator and a coax tee were added to impedance match the signal. This oscilloscope also possessed a serial port permitting computer control through a PC running Hameg’s proprietary software. This software was used to validate data being taken from cursor bars on the scope’s screen.

### Attenuators and Mounts

Two 5215 New Focus attenuators sat in front of the photodetectors (photodiode and CCD). These neutral density filters (Inconel coated) prevented both detectors from saturating. Also a high filter setting allowed the photodiode to function in the linear range.

Lens mounts, posts, and bases for this experiment came from commercial suppliers. These lens holders did not generate observable fluctuations in the data set through vibrations. The mount for the cavity was obtained from Lees. This

mount was utilized in a previous Advanced LIGO prototype experiment. This preceding experiment demanded stable cavity pointing for extended periods of time. The researchers implementing the mount found no observable motion in the device once it was set. This mount was deployed in this experiment.

Lens mounts for the probe laser's second mode matching telescope (MMT 2) were placed on New Focus 9801 five freedom stages with single axis New Focus translation stages on top. The five-freedom stage was used to align the final MMT lenses' optical axis to the beam. A translation stage allowed large axial translation ( $>2$  cm) while keeping the lens centered on the beamline. Micrometers on the translation stages and fine adjust screws on the five-freedom stages held the lenses without inadvertent sliding.

#### Power Meters and Laser Protection

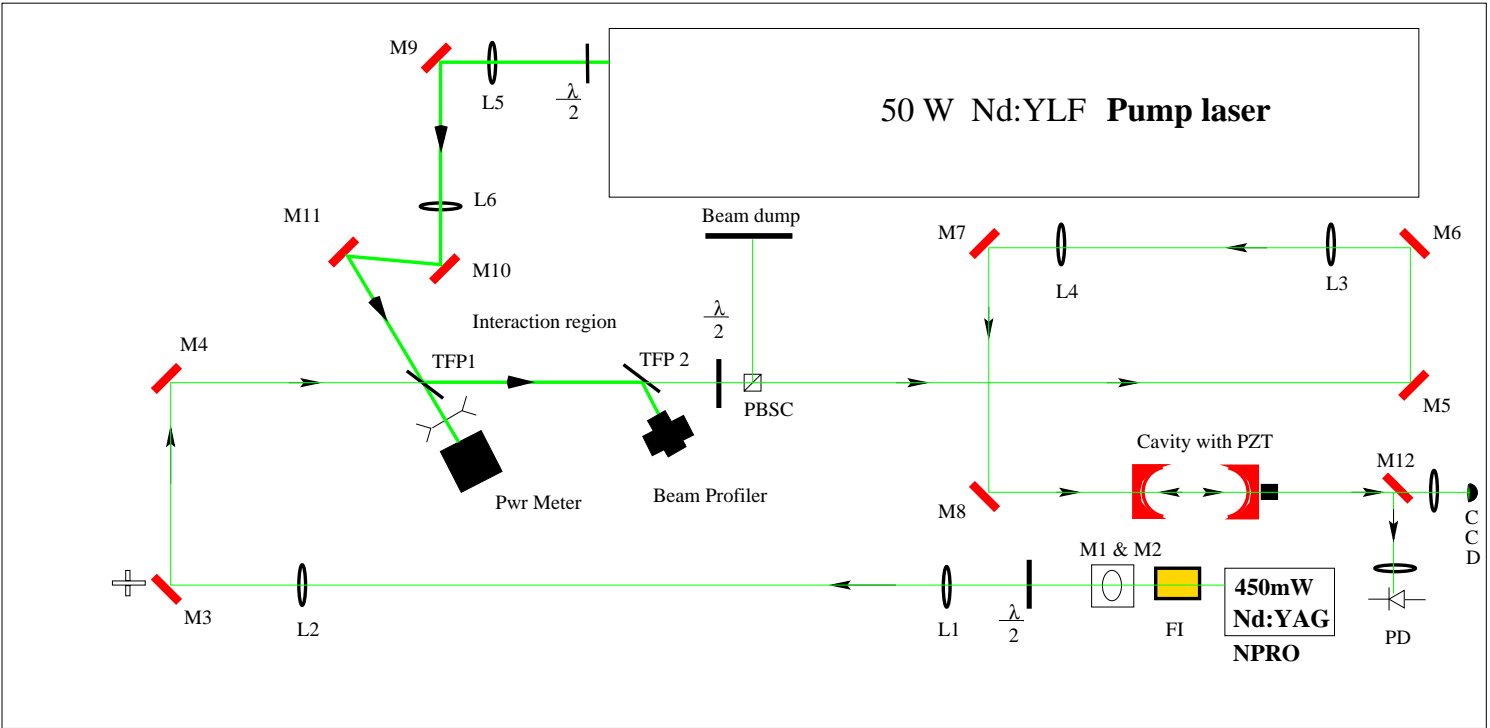
Two power meters were used in the experiment. ScienTech's S310 with an Ultra series pyroelectric head was used to measure the output of the high power pump laser. A highly defocussing lens was required to diffuse the beam to prevent detector damage. ScienTech's detector head had a 0 to 100 W range with a precision of  $\pm 0.1$  W. The second power meter was a Coherent 200 power meter rated for a maximum of 10 W. Both power meters showed delay times in their readout. ScienTech detector's time to lock was approximately 40 s to a couple of minutes depending on power differences. Coherent's detector locked onto a power reading within forty seconds.

Finally, steel plates (16 gauge) were bolted to the perimeter of the table. These plates served as a physical barrier to the pump laser should an optic misdirect the beam off the table. High temperature flat black paint minimized backscatter. Two anodized plates served as beam blocks in the event the pump or probe laser needed to be blocked without closing the shutter.

### 3.3.3 Beam Paths

After leaving the NPRO laser housing, the probe laser passed through EO-Tech's Faraday isolator. This isolator's input and output polarizers were positioned for maximum transmission. Next in the beamline was a vertical periscope that increased the probe beam height from 9 cm to 16.5 cm. This was the initial height of the pump laser; all equipment except EO-Tech's isolator was centered at 16.5 cm. A half-wave plate in a CVI rotational mount rotated the polarization for transmission through the interaction region's TFPs. The first mode matching telescope (MMT 1) followed this waveplate. Composed of a 250 mm lens and a 200 mm lens, this MMT developed a 1 mm waist within the center of the TGG crystal. A second pair of 45 degree incidence mirrors directed the beam through the interaction region, the test Faraday isolator. TFP 1 indicated the beginning of the interaction region. Incorrectly polarized probe beam deflected off TFP 1 into ScienTech's detector. The probe beam that flowed through the polarizer next encountered the Litton Faraday rotator and its TGG crystal. A 45 degree monolithic quartz rotator sat downstream of the TGG. Behind the 45 degree quartz rotator was the second TFP, TFP 2. The probe laser continued into a second half-wave plate and the polarizing beam splitter cube (PBSC). This suppressed any depolarized high power pump radiation that may have egressed on the probe laser's beamline. A third pair of mirrors redirected the probe beam into the second MMT. The second MMT (MMT 2) mode matched the probe beam into the cavity and was comprised of a 150 mm lens and a 125 mm lens. A fourth pair of mirrors sent the beam into the Fabry-Perot cavity for modal analysis. Modes that resonated were transmitted to a mirror. This mirror launched the probe beam through the New Focus attenuators, through a final focusing lens, and onto the ThorLabs photodiode. Light that transmitted through the mirror passed through an identical set of final optics before landing on the CCD camera.

Figure 3-9: A diagram of the experiment table.



The pump laser beamline was less complicated. The YLF laser first intercepted a half-wave plate. The half-wave plate and TFP 1 were used in combination to regulate the amount of high power radiation entering the interaction region. A split MMT (MMT 3) formed a waist coplanar with the probe laser within the TGG. One hundred millimeter and one hundred fifty millimeter lenses comprised the pump's MMT. However, a mirror was required to redirect the pump beam within the MMT due to design constraints. Following MMT 3 were a fifth pair of mirrors. These mirrors were used to direct the beam on TFP 1 at Brewster's angle and to align the pump coaxially with the probe beamline. Pump light that was not deflected into the interaction region entered the ScienTech power meter. The ScienTech detector head was placed here since the FK51 glass scattered some of the pump light. Placing the detector head near TFP 2 would have given false powers. Pump radiation that was deflected into the interaction region passed through the TGG crystal and quartz rotator. TFP 2 then deflected the pump laser into the BeamScan which was being used in coaxial alignment and beam quality control. Any depolarized pump light escaping towards the cavity was suppressed using the aforementioned half-wave plate and PBSC.

### 3.4 Procedures

#### 3.4.1 MMT Alignment Techniques

Setting the MMT lenses in the correct positions was simplified by utilizing the beam profiler's centroid tracking subroutine. This tracking program provided a reference point indicating the laser's original direction. A lens could then be positioned in front of BeamScan and translated until the laser fell on the reference point. It was possible that the beam could appear to travel through the reference point and be directed off the beamline due to beam width. To thwart this the BeamScan reference points at two positions on the beamline were acquired. When the laser propagated directly through the lens' optical center, centroid data at two

points along the beamline would show no lateral displacement on the centroid graphic user interface (GUI).

With the lenses installed in their appropriate positions, beam profilometry and a  $\chi^2$  fit provided information on propagated waist position and size. Should the beam be converging incorrectly the MMT was manually modified and another profile taken. Since the probe beam was elliptical, the mode matching calculations were based on the horizontal waist.

### 3.4.2 Overlap Alignment

Alignment of the pump laser on the probe laser was critical since the entirety of the thermal lens needed to be observed without excitation of the  $HG_{10}$  mode.<sup>k</sup> Mirrors M7, M8, and the cavity were rotated to suppress the  $HG_{10}$  mode into the noise floor (approximately 2 percent of the  $TEM_{00}$  mode). To correctly establish pointing, two working points<sup>l</sup> and a reasonably large working length<sup>m</sup> were required. The experiments two working points were the BeamScan, intercepting bounce light from TFP 2, and the CCD camera. This provided nearly 2.5 m of working distance or a theoretical 1 mrad pointing accuracy.<sup>n</sup>

A quarter-wave plate was set behind the quartz rotator allowing 10 W of pump laser to flow towards the cavity and 240 mW of probe light to enter BeamScan. The pump laser was then blocked without closing the shutter. The BeamScan's pointing feature was then centered on the probe beam indicating the

---

<sup>k</sup> The excitation of the  $HG_{10}$  mode indicated a pointing deflection generated by sensing a noncentered thermal lens.

<sup>l</sup> Two points are needed geometrically to form a straight line.

<sup>m</sup> Longer working lengths provide greater pointing resolution when handling small angles.

<sup>n</sup> This calculation was based on the BeamScan's best ability to detect lateral displacement.

short reference point. The probe light spot's center on the monitor noted the long reference point.

The probe beam was then stopped by a second block plate and the pump beam opened. Mirror M10 was used to walk the beam beyond the short reference point's center. Mirror M11 was then used to walk the beam through the circular symmetric modes to a clear laterally symmetric mode. The beam walking process was repeated until the pump laser's position indicator fell on the BeamScan's center crosshairs, and the shape of the pump laser through the cavity was circularized. This insured that the two beams were sharing the same volume of space. The quarter-wave plate was finally removed from the beamline.

### 3.4.3 Data Collection

Once the two beams were correctly aligned, the pump laser was set at 3.0 W and the pump's half-wave plate rotated to transmit all possible light through TFP 1. The pump laser was then brought to running capacity (52.0 W) and left to stabilize over 15 minutes. The probe laser and all electronics were allowed to thermally stabilize over 10 to 15 minutes. Thermal stabilization for the YLF was especially important as its power level would fluctuate  $\pm 0.5$  W until cooling water and lasing crystals reached an equilibrium temperature.

The statement all possible light implies that some light was polarized randomly with respect to the laser field. A couple hundred milliwatts of errant radiation entered the interaction region. This did not affect measurements at zero power. A measurement of  $TEM_{00}$  magnitude with and without the pump engaged showed no visible changes in the mode of the probe laser.

The TTi function generator was not needed in the data collection, only during alignment. Therefore, the generator was removed from the PZT. This provided operators to manually slew the cavity and to find the best resonance points.

Differences between maximum power and laser power on the ScienTech detector head indicated the amount of power entering the interaction region. Pump laser power levels were increased by 8 W increments until 52 W flowed through the interaction region. A wait time of 5 minutes was imposed to insure the thermalization of the TGG and to allow the ScienTech power meter to stabilize. Following each power increase, the amount of power entering and leaving the interaction region (probe beamline) was checked using the Coherent 200 detector on the 0.3 W and later the 1.0 W setting. This check would disclose any power loss or gain in the probe laser. Power fluctuations in the probe would have resulted in false lensing data. The check also provided data regarding thermally induced birefringence and TFP performance. Furthermore, the check provided information of the noise floor as pump power was increased.

Next the intensity of each visible mode was recorded. The CCD allowed the mode to be recognized on the display screen. Here the PZT driver's monotonic drifting characteristic became useful. The PZT driver would automatically drift through a resonant mode of when the DC offset positioned the output coupler at roughly 10 percent resonance. This method of drifting proved to be more effective than manually adjusting the DC offset to hold resonance. Manipulating the DC offset and watching for maximum intensity values on the oscilloscope resulted in overcompensation through human error.

One should note that as the cavity drifted through resonance the peak was not symmetric. As indicated in the first section of this chapter, circulating powers in the cavity forced the cavity off resonance rather quickly. For example, drifting into resonance often took tens of seconds. The "kick out" of resonance happened within a second. This occasionally gave lower intensity readings. However, several drift measurements remedied this problem.

The sum of all observable modes provided confirmation that the experiment was not losing or gaining light through depolarization or nonlinear effects. Nevertheless, the primary modes of interest were the fundamental  $TEM_{00}$  mode, the Laguerre-Gauss  $LG_{10}$  mode, and the Hermite-Gauss  $HG_{00}$  mode.

Once the control data run (TGG only) was complete, 6.8 cm of FK51 Schott glass was inserted behind the quartz rotator. A gap of 1 millimeter remained between the wedges. Mirrors M5 and M6 were adjusted to compensate for the beam displacement. The above procedures were repeated with the FK51 sitting in the beamline.

### 3.5 Absorption Coefficients

Absorption coefficients were acquired through a four-point method. This method involved observing incident, transmitted, front surface, and back surface reflected light levels. A focused probe beam,  $\omega_0 = 100 \mu\text{m}$ , entered the target crystal. A non-normal incidence angle provided the means to separate the reflected beams. To obtain the absorption coefficient, the transmitted and reflected beams were summed,

$$I_{t,r} = I_{transmitted} + I_{frontrefl} + I_{backrefl} \quad (3.22)$$

The difference between the sum and the incident radiation divided by the incident radiation gave the absorption factor. Dividing by the length,  $l$ , of the material yielded the absorption coefficient,

$$\alpha \cdot l = \frac{I_{incident} - I_{t,r}}{I_{incident}},$$

$$\alpha = \frac{\alpha \cdot l}{l}. \quad (3.23)$$

To obtain light intensities necessary for this computation, the ThorLabs battery powered photodiode was used to directly intercept the light. A Glan-Thompson polarizer, half-wave plate, and a PBSC prevented laser light from

saturating the photodiode. A block plate aided in differentiating between the two reflections. An MMT consisting of a 19.0 mm and 60 mm lens focused the probe beam. Absorption coefficient results are noted in chapter 2, section 7: The Wavefront Model.

### 3.6 Analysis

The results for the both uncompensated and compensated measurements are plotted below superimposed on the theoretical data curves seen in the chapter 2. One will note that the experimental uncompensated data points verify that laser power shifts dramatically due to the thermal lens in the TGG. Normalized intensity in the  $TEM_{00}$  mode falls from 1, perfect mode matching, to 60 percent at 50.2 W. The radius of the circles indicates approximately one sigma. With respect to the theoretical calculation and the empirical data, no fitting parameters were used during plotting. To obtain a correct fit, it was necessary to establish the absorption coefficients of the TGG and FK51. Absorption coefficients for TGG,  $\alpha_{TGG}$ , indicated that the Litton AirTronics sample exceeded  $\alpha$  factors found in literature by a factor of 3. This factor became important during the compensation tests with FK51.

Compensated data however told a slightly different story than what the theory pointed towards. Initial data runs showed the fundamental mode dropped qualitatively more slowly than the uncompensated data. At 50 W, the fundamental mode dropped to 87 percent of the  $TEM_{00}$  intensity value observed at zero incident pump power. However,  $HG_{10}$  exceeded 5.5 percent of the  $TEM_{00}$  intensity at 34.3 W. At full pump power, both  $HG_{10}$  and  $LG_{10}$  modes exceeded 9.5 percent of the  $TEM_{00}$  intensity.

The second compensation data run was performed by modifying the procedures. Following each increment in pump power, the probe beam was readjusted to minimize the  $HG_{10}$  mode. This realigned the probe beam and permitted an

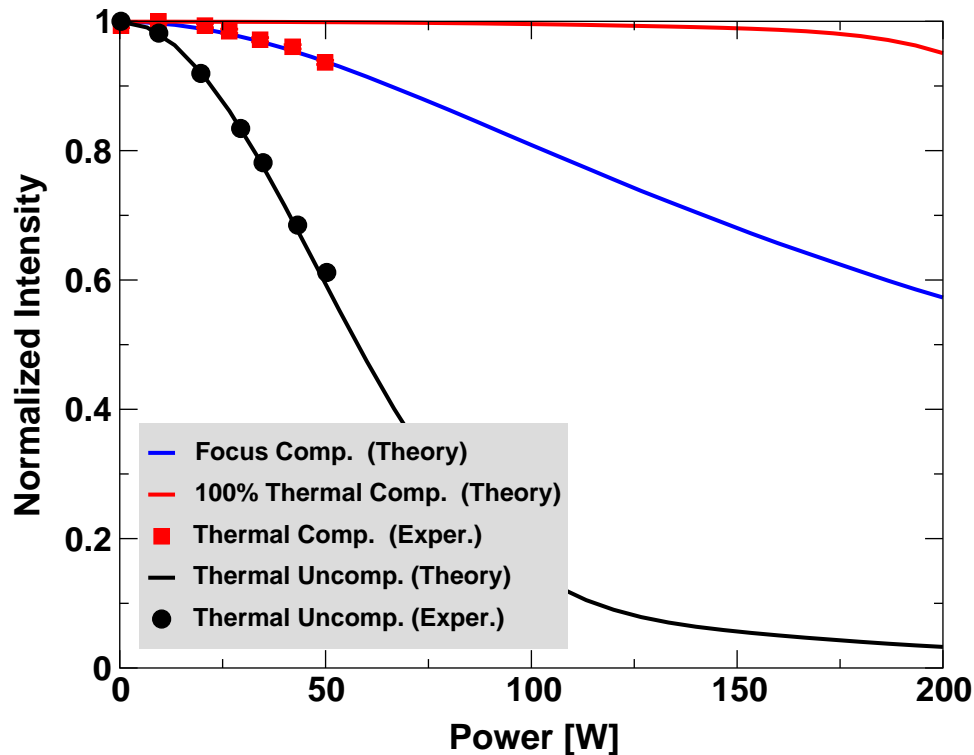


Figure 3–10: A plot of experimental data superimposed on Chapter 2’s theoretical results. The uncompensated thermal lensing data follows the predicted uncompensated line’s rapid fall off well. The compensated thermal lensing data however appear to track the focus compensated curve instead of the red thermal compensation curve. This mismatch was determined to result from the lack of FK51 glass interacting with the distorted laser beam. No fitting parameters were applied; datum point size is representative of the error bars.

increased visibility of the axial mode shift,  $LG_{10}$ . Results using the modified procedures indicated a retention of  $TEM_{00}$  mode. At 50 W the normalized intensity  $TEM_{00}$  intensity falls to 93.6 percent. The  $HG_{10}$  to  $TEM_{00}$  and  $LG_{10}$  to  $TEM_{00}$  ratios crested at 1.3 percent and 8.7 percent at 50 W. Since the amount of higher order modes showed no significant increase beyond the initial FK51 data run, we conclude that the  $HG_{10}$  excitation was caused by the glass’s wedge geometry and nonuniform thermal boundary conditions. Furthermore, the change in  $LG_{10}$  is minimal. Therefore, this implies that the second compensated data set would have been obtained in the initial data run if the wedges had not displaced the probe

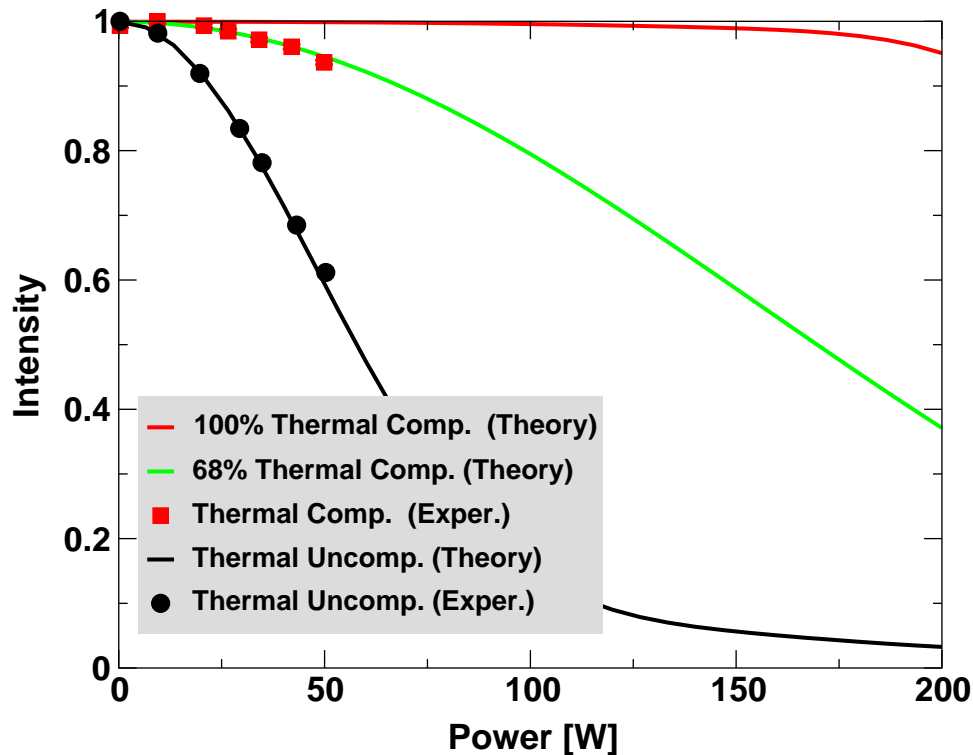


Figure 3–11: A plot of experimental data superimposed on Chapter 2’s theoretical results. The green line represents 68 percent compensation superimposed on the experimental compensation data. The focus compensation curve has been removed. No fitting parameters were applied; datum point size is representative of the error bars.

beam. According to theoretical compensation curves state that fundamental mode intensity should remain above 99 percent at approximately 50 W and fall to 95 percent at 200 W.

The reason for the lack of optimum compensation arises in the aforementioned  $\alpha_{TGG}$ . Being a factor 3 greater than what literature records, the data indicates that the length of FK51 glass used in the experiment was not enough to perform the calculated task. A modification to the computer model’s glass length shows that this experiment had achieved 68 percent of first order compensation limit. In terms of length, 3 cm more glass would have compensated the thermal lens in the TGG.

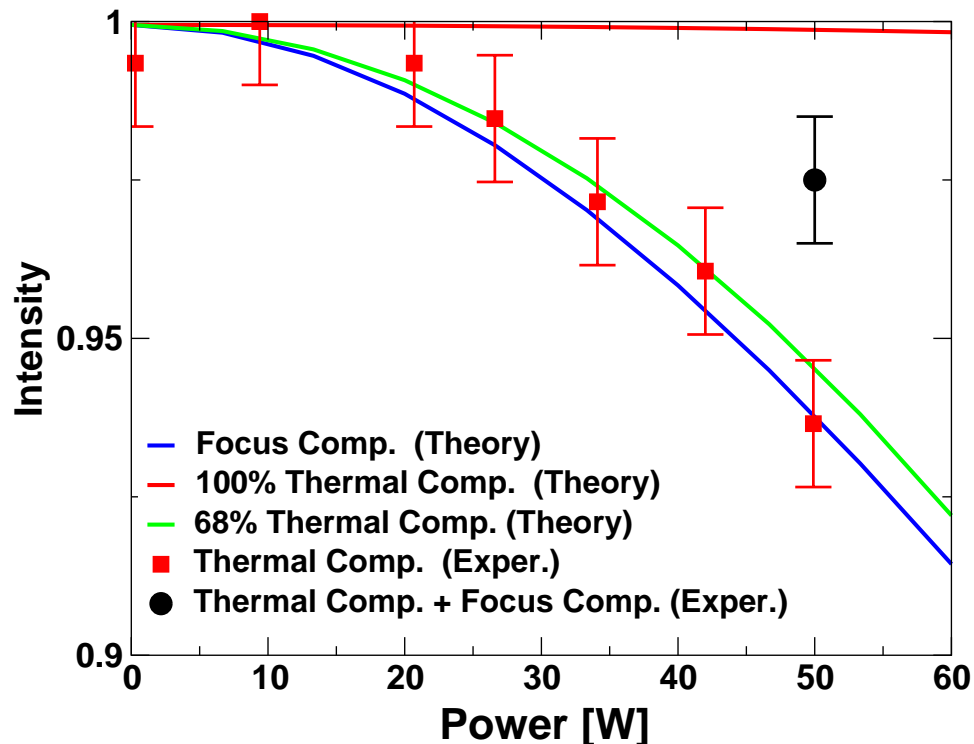


Figure 3-12: A zoom-in of the data plot shows that the thermally compensated data in this experiment follow a 68 percent compensation curve. The solitary black point was obtained through refinement of the final mode matching telescope, lenses L3 and L4. This refinement increased modal restoration to 97 percent.

To verify that this experiment did not simply perform a focus compensation,<sup>o</sup> MMT 2 was altered to improve mode matching with the cavity following FK51 data acquisition. At maximum incident power the new point increased to 97 percent. This was 3.4 percent greater than the 50 W FK51 data point and 4 percent greater than the focus compensated data point. All datum error bars span approximately 1 percent. Therefore, it can be concluded that this maximization was attributed primarily to spatial mode compensation.

<sup>o</sup> Focus compensation implies that higher order transverse modes are still intact.

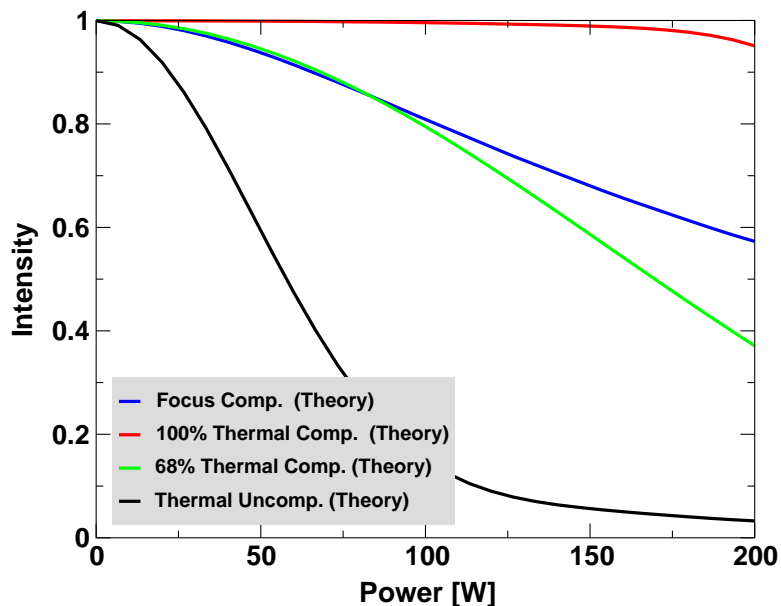


Figure 3–13: An overlay of the 68 percent compensation curve and the focal compensation curve. One can see that the two curves track each other until 60 W. After this point compensation bows to focal compensation techniques.

The model notes that for optimum compensation, a point solution must be found for each TGG crystal. However, MMT 2’s ability to improve compensation would allow an error margin to exist for designers of mode critical systems.

Throughout the experiment tilt modes did not exceed 3.4 percent for the TGG data run. The FK51 faired better with a maximum tilt of 1.3 percent. This pointed out that the alignment of the pump on probe was concentric to within 5 percent of the probe beam radius.

Power data taken immediately upstream and downstream of the interaction region disclosed two intriguing results regarding depolarization. Although the probe laser light did not fluctuate more than 3.5 percent, pump light leaking through TFP 2 increased by 20 percent when only the TGG sat in the beamline. The FK51 increased the pump leakage by nearly 3-fold. This depolarization of the light field was attributed to thermally induced birefringence. At mid-range pump powers, a clear “clover leaf” mode was visible on frequency doubling ceramic

sensors. This was the definite verification of the stress induced depolarization. However, it was not entirely clear why probe light was not as greatly influenced.

## CHAPTER 4 CONCLUSION

### 4.1 Results

This experiment has demonstrated a viable passive method for counteracting thermal lenses in Faraday isolators. By exploiting the thermal dependence of the index of refraction, we are able to experimentally recover more than 93 percent of the original laser mode at 50 W pump power. It must be emphasized that this is a point solution for each TGG crystal. An optimized solution would permit future gravitational wave detectors to have numerous highly effective alignment and working points. During alignment at 20 W, Advanced LIGO would observe nearly 100 percent mode matching. Following the increase to full running power, Advanced LIGO's core optics would retain 97.5 percent of the light in the  $TEM_{00}$  mode. However, an MMT downstream of the compensated Faraday isolator can improve mode matching should the glass not be of appropriate length.

### 4.2 Future Experiments

Future studies into passive compensation should include applications to other long input optics such as those found in electro-optic modulators. Also thermally induced birefringence must be studied as a function of incident light intensity. As indicated by the power data taken before and after the interaction region, pump light was depolarized and proceeded towards the cavity. Although it may not resonate in the core optics, this process does remove light from the fundamental mode and may effect final results.

Data acquired in April 2002 indicated that FK51 has a depolarization coefficient of the same magnitude of TGG. Due to FK51's glass characteristic, axial rotation will have no effect in counteracting depolarization as it has in IAP Faraday

rotators<sup>a</sup>. Most important, as an optical diode, thermally induced birefringence can readily defeat an isolator's ability to decouple subsystems. Finally, temperature and the varying of boundary conditions of the FK51 should be considered. This experiment relied on large pieces of freestanding glass. These pieces were not uniformly cooled since one side conducted heat to its pedestal and the other four sides released heat through convection. Ultimately designs for compensated Faraday isolators may demand smaller rod shapes to minimize the cost of glass, and thermal control of the glass could provide a negative focus adaptive optic.

Another possibility for compensating the thermal lens generated by TGG crystals may lie in optical gels. Gels that are used to index match fibers possess  $dn/dT$ 's that are two orders of magnitude greater than the FK51 glass tested. This implies that if applicable, these compensation materials could be placed closer to the crystal of interest (TGG). Placing the compensating medium closer to the thermal lens reduces the Gouy phase shift. This increases the incident laser power that the isolator can tolerate without the losing an excessive amount of  $TEM_{00}$  mode. However, this assumes that the  $dn/dT$  term will remain the dominant term in the  $\Delta OPL$  sum. The introduction of gels removes the possibility of thermally induced birefringence. These gels also show large expansion coefficients. This may increase the complexity of optimum compensation.

---

<sup>a</sup> IAP Russia at Nihzny Novogrod has compensated thermally induced birefringence in TGG by rotating one crystal axially by 45 degrees with respect to its counterpart.

APPENDIX A  
COMPLEX-Q AND THE ABCD LAW

A.1 Derivation of q

Chapter 3.2.1 started to demonstrate the difficulties of full wavefront propagation. The scheme of using the full Fresnel-Kirchoff integral equation in an unconfined region becomes increasingly difficult. A less precise but more convenient method of field propagation utilizes components of the phase factor obtainable through the wave equation [28, 29]. This term is referred to as the “complex-q.”

We assume that the laser phase front shape changes slowly with respect to the  $z$ -axis (the direction of propagation). We also assume that the laser’s intensity profile is Gaussian and that the paraxial approximation applies [28, 29]. With these assumptions we can begin our derivation with the wave equation,

$$\left(\nabla^2 - \frac{1}{c^2} \frac{\partial^2}{\partial t^2}\right) U(x, y, z, t) = 0. \quad (\text{A.1})$$

Using separation of variables we can break the equation into a time and space differential equations,

$$U(x, y, z, t) = u(x, y, z)T(t). \quad (\text{A.2})$$

The space term becomes

$$\nabla^2 u(x, y, z) - k^2 u(x, y, z) = 0. \quad (\text{A.3})$$

The time terms becomes

$$\frac{1}{c^2} \frac{\partial^2}{\partial t^2} T(t) - k^2 T(t) = 0. \quad (\text{A.4})$$

The time component has the familiar harmonic solution of

$$T(t) = T_0 e^{-i\omega t}. \quad (\text{A.5})$$

This part of the solution behaves as a simple multiplier to the space term. Therefore the time component will not be carried through the rest of this solution.

To solve the space differential equation we assume a solution that looks like

$$u(x, y, z) = \Phi(x, y, z) e^{-ikz}. \quad (\text{A.6})$$

Expanding the differential equation we obtain

$$\left( \frac{\partial^2 \Phi}{\partial x^2} + \frac{\partial^2 \Phi}{\partial y^2} \right) - i2k \frac{\partial \Phi}{\partial z} = 0. \quad (\text{A.7})$$

We can assume a solution of the following form

$$\Phi = e^{-i(P(z) + \frac{k}{2q} r^2)}. \quad (\text{A.8})$$

where  $P(z)$  is a complex phase shift,  $k = \frac{2\pi}{\lambda}$ ,  $r^2 = x^2 + y^2$ , and  $q = q(z)$ .

Let's focus on the second phase shift,

$$\Phi_q = e^{-i \frac{k}{2q} r^2}. \quad (\text{A.9})$$

Since this portion of the model is to represent the laser field's Gaussian amplitude profile  $q$  must be imaginary [28]. We also know that the Gaussian profile's characteristic length is the waist length,  $\omega_0$  [29]. Therefore, the form of  $q$  at the laser waist is

$$q_0 = -\frac{i\pi\omega_0^2}{\lambda}. \quad (\text{A.10})$$

By sending the solution through the differential equation we can determine what the phase parameters are. Written below is the full expansion of the

differential equation,

$$\begin{aligned}
& -i\frac{k}{q}e^{-i(P(z)+\frac{k}{2q}x^2+\frac{k}{2q}y^2)} - \frac{k^2}{q^2}x^2e^{-i(P(z)+\frac{k}{2q}x^2+\frac{k}{2q}y^2)}, \\
& -i\frac{k}{q}e^{-i(P(z)+\frac{k}{2q}x^2+\frac{k}{2q}y^2)} - \frac{k^2}{q^2}y^2e^{-i(P(z)+\frac{k}{2q}x^2+\frac{k}{2q}y^2)}, \\
& -2kP'(z)e^{-i(P(z)+\frac{k}{2q}x^2+\frac{k}{2q}y^2)} + \frac{k^2}{q^2}q'(x^2+y^2)e^{-i(P(z)+\frac{k}{2q}x^2+\frac{k}{2q}y^2)} = 0. \tag{A.11}
\end{aligned}$$

If we separate this equation through powers of  $k$  we obtain the following:

1.

$$\begin{aligned}
& -\frac{k^2}{q^2}x^2e^{-i(P(z)+\frac{k}{2q}x^2+\frac{k}{2q}y^2)} - \frac{k^2}{q^2}y^2e^{-i(P(z)+\frac{k}{2q}x^2+\frac{k}{2q}y^2)} \\
& + \frac{k^2}{q^2}q'(x^2+y^2)e^{-i(P(z)+\frac{k}{2q}x^2+\frac{k}{2q}y^2)} = 0; \tag{A.12}
\end{aligned}$$

2.

$$\begin{aligned}
& -i\frac{k}{q}e^{-i(P(z)+\frac{k}{2q}x^2+\frac{k}{2q}y^2)} - i\frac{k}{q}e^{-i(P(z)+\frac{k}{2q}x^2+\frac{k}{2q}y^2)} \\
& -2kP'(z)e^{-i(P(z)+\frac{k}{2q}x^2+\frac{k}{2q}y^2)} = 0. \tag{A.13}
\end{aligned}$$

This implies

1.  $q' = 1$  ;
2.  $P'(z) = -\frac{i}{q}$  .

Integrate item 1 with respect to  $z$ ,

$$q(z) = q_0 + z. \tag{A.14}$$

This simple addition law indicates how one can propagate a complex- $q$  factor in free space [29, 28]. The logic for this will become apparent in the following section.

Inserting this into item 2 we acquire

$$P'(z) = -\frac{i}{q(z)}, \quad (\text{A.15})$$

$$iP(z) = \ln \left( z + \frac{i\pi\lambda}{\pi\omega_0^2} \right) + C', \quad (\text{A.16})$$

$$P(z) = \ln \sqrt{1 + \left( \frac{\lambda z}{\pi\omega^2} \right)^2} - i \arctan \frac{\lambda z}{\pi\omega_0^2}. \quad (\text{A.17})$$

The first term represents the phase difference between a plane wave and a Gaussian phase front. The imaginary coefficient is the Gouy phase shift [28]. This component models the phase shift as the laser's wavefront travels through a waist.

### A.2 ABCD Laws for Gaussian Laser Propagation

Gaussian lasers are propagated through the ABCD law,

$$q_1(z) = \frac{Aq_0(z) + B}{Cq_0(z) + D}. \quad (\text{A.18})$$

This formalism acquires its four terms (A, B, C, and D) from  $2 \times 2$  matrices implemented in ray optics. The derivation for the ABCD law in Gaussian optics is as follows.

In the thin lens approximation, a lens of focal length  $f$  effects a spherical wavefront's radius of curvature in the following form

$$\frac{1}{R'(z)} = \frac{1}{R(z)} - \frac{1}{f}. \quad (\text{A.19})$$

This is applicable for Gaussian laser phasefronts provided the lens is thin enough that it does not greatly alter the transverse radius of the laser beam,

$$\frac{1}{q_1(z)} = \frac{1}{q_0(z)} - \frac{1}{f}. \quad (\text{A.20})$$

This indicates that the complex- $q$  is the phasefront's radius of curvature in the complex plane [28, 29].

Combining this with free space propagation (item 1 of section A.1),

$$q_1(z) = q_0(z) + z, \quad (\text{A.21})$$

and then propagating the beam again, we acquire

$$q(z) = \frac{(1 - \frac{z_2}{f})q_0(z) + (z_1 + z_2 - \frac{z_1 z_2}{f})}{(-\frac{1}{f})q_0 + (1 - \frac{z_1}{f})}. \quad (\text{A.22})$$

Looking at the coefficients of  $q_0(z)$  in the form of the ABCD law, we find that the coefficients are the same as the four elements in the  $2 \times 2$  matrix utilized by ray optics to move a ray through a thin lens,

$$M_z = \begin{pmatrix} 1 & z \\ 0 & 1 \end{pmatrix},$$

$$M_f = \begin{pmatrix} 1 & 0 \\ -\frac{1}{f} & 1 \end{pmatrix},$$

$$\begin{aligned} M_{tot} &= M_{z2} \cdot M_f \cdot M_{z1}, \\ &= \begin{pmatrix} (1 - \frac{z_2}{f}) & (z_1 + z_2 - \frac{z_1 z_2}{f}) \\ -\frac{1}{f} & (1 - \frac{z_1}{f}) \end{pmatrix}. \end{aligned} \quad (\text{A.23})$$

A list of ABCD matrices can be found in Siegman, Fowles, Hodgson and Weber, and many other optics book.

This coincidence occurs because both ray optics and paraxial wave analysis track the phasefront's radius of curvature utilizing the thin lens approximation.

$$\begin{pmatrix} r' \\ \theta' \end{pmatrix} = \begin{pmatrix} A & B \\ C & D \end{pmatrix} \begin{pmatrix} r \\ \theta \end{pmatrix}. \quad (\text{A.24})$$

The radius of curvature for a spherical wavefront in ray optics becomes

$$R' = \frac{r'}{\theta'} = \frac{Ar + B}{Cr + D}. \quad (\text{A.25})$$

We can now see that the complex- $q$  is merely the complex radius of curvature of the laser's wavefront<sup>a</sup> .

---

<sup>a</sup> Walther [29] presents a similar but more generalized approach in his book.

## APPENDIX B JONES MATRICES

The polarization of an electromagnetic field represents the direction that the plane in which the electric field is directed. This polarization can be represented by a  $2 \times 1$  vector. Changes in polarization angle due to interactions with various media (dust, interfaces, magneto-optics, etc.) can be modeled through a change of basis using a  $2 \times 2$  matrix called Jones matrices [14, 22].

The formalism for this interaction is as follows

$$\begin{pmatrix} P'_x \\ P'_y \end{pmatrix} = \begin{pmatrix} M_{11} & M_{12} \\ M_{21} & M_{22} \end{pmatrix} \begin{pmatrix} P_x \\ P_y \end{pmatrix} \quad (\text{B.1})$$

where  $P'_x$  and  $P'_y$  are the new electric field polarization magnitudes in the orthogonal directions, the matrix  $M$  is the change in direction of polarization due to the interaction with some set of media, and the final  $P$  vector is the original component magnitudes of the electric field [14, 22].

For example, let's start with a electromagnetic wave completely polarized in the  $x$ -axis. This wave interacts first with a quarter-wave plate,  $QWP$ , that has been rotated by  $45^\circ$  with respect to the incoming light's polarization and then a polarizer set to pass  $y$  polarized light. To find the final vector amplitude, we multiply the matrices right to left in the order that our electromagnetic field "sees" the optical components,

$$M_{QWP} = \frac{1}{\sqrt{2}} \begin{pmatrix} 1 & i \\ i & 1 \end{pmatrix}, \quad (\text{B.2})$$

$$M_{Pol} = \begin{pmatrix} 0 & 0 \\ 0 & 1 \end{pmatrix}, \quad (\text{B.3})$$

$$\begin{aligned} M_{final} &= M_{pol}M_{QWP} \\ &= \frac{1}{\sqrt{2}} \begin{pmatrix} 0 & i \\ 0 & 1 \end{pmatrix}, \end{aligned} \quad (\text{B.4})$$

$$\frac{1}{\sqrt{2}} \begin{pmatrix} i \\ 1 \end{pmatrix} = \begin{pmatrix} 0 & i \\ 0 & 1 \end{pmatrix} \begin{pmatrix} 1 \\ 0 \end{pmatrix}. \quad (\text{B.5})$$

The solution obtained indicates that the resulting light is right circularly polarized.

This rather trivial exercise demonstrates that the Jones matrices for optical components can be multiplied in the order of observation. Furthermore, it is relatively simple to analyze the resulting polarization direction through the component magnitudes. Further information and a full list of Jones matrices for optical components can be found in nearly any modern optics textbook (for example, Hodgson and Weber, Fowles, or Siegman).

APPENDIX C  
UF THERMAL LENSING CODE

```
%%%%%%%%%%%%%%%%%%%%%%%%%%%%%%%%%%%%%%%%%%%%%%%%%%%%%%%%%%%%%%%%%%%%%%%%
%Master.m %Written for UF-LIGO
%Author Guido Mueller 28 October 2001
%Comments by Rupal S. Amin // MatLAB-Octave Code
%%%%%%%%%%%%%%%%%%%%%%%%%%%%%%%%%%%%%%%%%%%%%%%%%%%%%%%%%%%%%%%%%%%%%%%%

%%%%%%%%%%%%%%%%%%%%%%%%%%%%%%%%%%%%%%%%%%%%%%%%%%%%%%%%%%%%%%%%%%%%%%%%
% MAIN
% All lengths in millimeters
%%%%%%%%%%%%%%%%%%%%%%%%%%%%%%%%%%%%%%%%%%%%%%%%%%%%%%%%%%%%%%%%%%%%%%%%
lambda = 1.064e-3; %Wavelength of laser
P_max=200; %Maximum power of laser [W]
L = 30; %The distance between the two slabs

%Load crystal and glass parameters
crystal_1_params; %Input TGG crystal parameters.
crystal_2_params; %Input FK51 glass parameters.

w_in = 1; %Laser waist size in TGG
invR_in = 0; %Radius of curvature of wavefront at the waist

c_1=zeros(19,1); %Initialize constant array.
```

```



```

```

%Calculate the sum for each of the 201 points on the (transverse) x-axis.
for step=1:num_step
    sum=0;
    fac=1;
    %Octave does not have a "factorial(n)" function.
    for l=1:m
        fac = fac*l;
        sum = sum+(-1)^l*(2*r^2/w_in^2)^l/(l*fac);
    end
    Lambda(step) = sum;
    pos(step) = r; %Keep track of transverse position
    %Increment to the next position on the x-axis.
    r=r + delta/num_step;
end

%axis([0,4]);
%plot(pos,Lambda);

pow_step = 31; %The laser power will be increased in 30 steps.

dP=P_max/(pow_step-1); %Determine power step size
P=0; %Initialize laser power variable

P_out = zeros(4,pow_step); %Initialize mode intensity matrix
%%%%%%%%%%%%%%%%%%%%%%%%%%%%%%%%%%%%%%%%%%%%%%%%%%%%%%%%%%%%%%%%%%%%%%%%
%Start solving for Laguerre-Gauss mode series constants through 30 power
% increments.

```

```

%%%%%%%%%%%%%%%%%%%%%%%%%%%%%%%%%%%%%%%%%%%%%%%%%%%%%%%%%%%%%%%%%%%%%%%%
for k=1:pow_step

P = P+dP; % Step up the power!

%The thermal lens's delta OPL coefficients.
coef_1 = a_1*P/(4*pi*k_1) * dn_dT_1 * L_1;
coef_2 = a_2*P/(4*pi*k_2) * dn_dT_2 * L_2;

%Multiply the above coefficients by the optical pathlength distortion
% arrays.
Lambda_1 = coef_1 * Lambda;

%The second coefficient is set to be negative the first coefficient.
%This enables us to obtain optimum compensation.
coef_2 = -coef_1;

Lambda_2 = coef_2 * Lambda;

%Call the "radial_lens" subroutine.
[c_1,P_out(3,k),invR_eff]
    = radial_lens(q_1, num_step, delta, Lambda_1, lambda);

%Call the "focus_comp" subroutine.
[P_out(3,k), invR_eff, invR_app]
    = focus_comp(q_1, num_step, delta, Lambda_1,lambda);

%Calculate the absolute intensity output for all modes.

```

```

P_out(2,k)= abs(c_1(1)).^2;

%Detemine the optical distance from the TGG to FK51 glass.
d_dif = L_1/(2*n_1)+L+L_2/(2*n_2);

%Determine the complex q coming out of the TGG
p_2 = (invR_eff+i*imag(1/q_1))^(1)+d_dif;

w_2 = sqrt(-lambda/(pi*imag(1/p_2)));

q_2 = q_1+d_dif;

%Call "radial_gouy" to propagate the wavefront to the FK51 glass.
c_3 = radial_gouy(c_1,q_2);

w_ave = (w_in+w_2)/2;

% Calculate the coefficient of the FK51 glass
%(removed for optimum comp)
%coef_2 = a_2*P/(4*pi*k_2) * dn_dT_2 * L_2;
coef_2 = -coef_1;%*0.68;

Lambda_2 = coef_2 * Lambda;

%Call the "radial_correc" subroutine.
c_4 = radial_correc(c_3,q_in, num_step, delta, Lambda_2,lambda);

%Detemine the intensity of the compensated modes.

```

```

P_out(4,k) = abs(c_4)^2;
%Input incident power into "power" matrix
P_out(1,k) = P;

end

%P_out = P_out; %one dimensional analysis,
                %second dim gives additional losses

%Plot and write data to a file.
plot(P_out(1,:),P_out(2,:),P_out(1,:),
      P_out(3,:), P_out(1,:),P_out(4,:));

fid = fopen('result','w');
format_string = ['%.6e', '\t%.6e' , '\t%.6e' , '\t%.6e' , '\n'];
fprintf(fid, format_string , P_out);
fclose(fid)

%%%%%%%%%%%%%%%%%%%%%%%%%%%%%%%%%%%%%%%%%%%%%%%%%%%%%%%%%%%%%%%%%%%%%%%%
%Subroutine: radial_lens.m
%Thermal lensing subroutine implementing the phase shift due to the
% first crystal.
%Input variables:q_1, num_step, delta, Lambda_1, lambda
%Output variables:c_1: Laguerre-Gauss amplitude coefficients
%                P_un: power in phase front
%                invR_eff: 1/(effective radius of curvature ) used in focus

```

```

%                               compensation
%%%%%%%%%%%%%%%%%%%%%%%%%%%%%%%%%%%%%%%%%%%%%%%%%%%%%%%%%%%%%%%%%%%%%%%%
function [c_out,P_un,invR_eff] = radial_lens(q_in,num_step,delta,Lambda,lambda)

w = sqrt(-lambda/(pi*imag(1/q_in))); %Recalculate the input waist.

c_out = zeros(19,1); %Initialize array to hold modal amplitudes
P_un = 0;    %Initialize power variable

k_w = abs(round(w*num_step/delta));
%Approximate the radius of curvature of the Gaussian wavefront.
invR_eff = (2*(Lambda(k_w)-Lambda(num_step/2)))/w^2;

r = delta/num_step; %Radial position

LG = zeros(1,20); %Initialize Laguerre-Gauss weights.

for step=1:num_step
%u = Gaussian phase front distribution at the "step"
%    point with the thermal phase shift.
%v = Gaussian phase front distribution at the "step"
%    point without the thermal phase shift.
    u = (2/pi)^(1/2)*1/w*exp(-r^2/w^2)*exp(i*2*pi*Lambda(step)/lambda);
    v = (2/pi)^(1/2)*1/w*exp(-r^2/w^2)*exp(i*pi*r^2*invR_eff/lambda);

%Enter LG radial coordinate.
    y = 2*r^2/w^2;

```

```

%Generate 19 LG mode computations

    LG(1) = 1;
    LG(2) = 1-y;
    LG(3) = (2-4*y+y^2)/2;
    for n=3:19
        LG(n+1) = ((2*n-1-y)*LG(n)-(n-1)*LG(n-1))/n;
    end

%Input the Gaussian mode amplitude at transverse point r.
    u_0 = (2/pi)^(1/2) * 1/w *exp(-r^2/w^2);
%Calculate all amplitude coefficients.
% u = u_0*LG(1);
    c_out(1) = c_out(1)+ conj(u_0*LG(1)) * u* r * delta/num_step;

% u = u_0*LG(2);
    c_out(2) = c_out(2)+ conj(u_0*LG(2)) * u* r * delta/num_step;

% u = u_0*LG(3);
    c_out(3) = c_out(3)+ conj(u_0*LG(3)) * u* r * delta/num_step;

% u = u_0*LG(4);
    c_out(4) = c_out(4)+ conj(u_0*LG(4)) * u* r * delta/num_step;

% u = u_0*LG(5);
    c_out(5) = c_out(5)+ conj(u_0*LG(5)) * u* r * delta/num_step;

% u = u_0*LG(6);

```

```
c_out(6) = c_out(6)+ conj(u_0*LG(6)) * u* r * delta/num_step;

% u = u_0*LG(7);
c_out(7) = c_out(7)+ conj(u_0*LG(7)) * u* r * delta/num_step;

% u = u_0*LG(8);
c_out(8) = c_out(8)+ conj(u_0*LG(8)) * u* r * delta/num_step;

% u = u_0*LG(9);
c_out(9) = c_out(9)+ conj(u_0*LG(9)) * u* r * delta/num_step;

% u = u_0*LG(10);
c_out(10) = c_out(10)+ conj(u_0*LG(10)) * u* r * delta/num_step;

% u = u_0*LG(11);
c_out(11) = c_out(11)+ conj(u_0*LG(11)) * u* r * delta/num_step;

% u = u_0*LG(12);
c_out(12) = c_out(12)+ conj(u_0*LG(12)) * u* r * delta/num_step;

% u = u_0*LG(13);
c_out(13) = c_out(13)+ conj(u_0*LG(13)) * u* r * delta/num_step;

% u = u_0*LG(14);
c_out(14) = c_out(14)+ conj(u_0*LG(14)) * u* r * delta/num_step;

% u = u_0*LG(15);
```

```

c_out(15) = c_out(15)+ conj(u_0*LG(15)) * u* r * delta/num_step;

% u = u_0*LG(16);
c_out(16) = c_out(16)+ conj(u_0*LG(16)) * u* r * delta/num_step;

% u = u_0*LG(17);
c_out(17) = c_out(17)+ conj(u_0*LG(17)) * u* r * delta/num_step;

% u = u_0*LG(18);
c_out(18) = c_out(18)+ conj(u_0*LG(18)) * u* r * delta/num_step;

% u = u_0*LG(19);
c_out(19) = c_out(19)+ conj(u_0*LG(19)) * u* r * delta/num_step;

%Integrate the "power" in the phasefront.
P_un = P_un + conj(v) * u * r * delta/num_step;
r = r + delta/num_step; %Increment the radial coordinate.

end

%LG
%Calculate the amplitude over 2 pi radians
c_out = 2*pi*c_out;
%Calculate the intensity in the uncompensated
%phasefront
P_un = abs(2*pi*P_un)^2;

```

```

%%%%%%%%%%%%%%%%%%%%%%%%%%%%%%%%%%%%%%%%%%%%%%%%%%%%%%%%%%%%%%%%%%%%%%%%
%Subroutine: focus_comp.m
%This subroutine determines the extent that a laser can be repaired by a
%simple lens in the first order. This is NOT true compensation.
%Input variables:q_in, num_step, delta, Lambda,lambda (same as above)
%Output variables: P_un,invR_eff (same as above)
%
%           invR_app (returned for use in a modified thermal lensing
%
%                   code)
%%%%%%%%%%%%%%%%%%%%%%%%%%%%%%%%%%%%%%%%%%%%%%%%%%%%%%%%%%%%%%%%%%%%%%%%
function [P_un,invR_eff,invR_app] = focus_comp(q_in, num_step,
delta,Lambda,lambda)

w = sqrt(-lambda/(pi*imag(1/q_in))); %Calculate beam radius

% Initialize P_un array
P_un_1 = 0;
P_un_2 = 0;
P_un_3 = 0;
P_un_4 = 0;
P_un = 0;
P_app = 0;

% Determine the radius of curvature of the beam.
k_w = abs(round(w*num_step/delta));
invR_app = 2*Lambda(k_w)/w^2;
invR_eff=invR_app;
P_0 = 0;

```

```

P_1 = 0;
r = delta/num_step;

invR_p = 2*Lambda(k_w+1)/w^2;

% Determine the best Gauss mode that will fit the radius
%of curvature of the distorted beam
for step=1:num_step
    u = (2/pi)^(1/2)*1/w*exp(-r^2/w^2)*exp(i*2*pi*Lambda(step)/lambda);
    v_0 = (2/pi)^(1/2)*1/w*exp(-r^2/w^2)*exp(i*pi*r^2*invR_app/lambda);
    v_p = (2/pi)^(1/2)*1/w*exp(-r^2/w^2)*exp(i*pi*r^2*invR_p/lambda);

    P_0 = P_0 + conj(v_0) * u * r * delta/num_step;
    P_1 = P_1 + conj(v_p) * u * r * delta/num_step;
    r = r + delta/num_step;
end

P_0 = abs(2*pi*P_0)^2;
P_1 = abs(2*pi*P_1)^2;

dP = P_1 - P_0;

if dP > 0
    dir =1;
else
    dir = -1;
end

```

```

m=1;
r = delta/num_step;

P_1 = 0;

dP = 1;

k=0;

while dP>0

    k=k+1;

    invR_1 = 2*Lambda(k_w+dir*m)/w^2;

    for step=1:num_step

        u = (2/pi)^(1/2)*1/w*exp(-r^2/w^2)*exp(i*2*pi*Lambda(step)/lambda);
        v_1 = (2/pi)^(1/2)*1/w*exp(-r^2/w^2)*exp(i*pi*r^2*invR_1/lambda);

        P_1 = P_1 + conj(v_1) * u * r * delta/num_step;
        r = r + delta/num_step;

    end

    P_1 = abs(2*pi*P_1)^2;
    dP = P_1 - P_0;

```

```

if dP > 0
    m=m+1;
    P_0=P_1;
    invR_eff = invR_1;
    P_1 = 0;
end
r = delta/num_step;
if k>25
    dP = -1;
end
end

P_un = P_0^2; %Record intensity

%%%%%%%%%%%%%%%%%%%%%%%%%%%%%%%%%%%%%%%%%%%%%%%%%%%%%%%%%%%%%%%%%%%%%%%%
%Subroutine: radial_gouy.m
%This subroutine obtains the appropriate Gouy
%phase shifts for a beam going through a focus.
%Input variables:c_in, q_in
%Output variables:c_out
%%%%%%%%%%%%%%%%%%%%%%%%%%%%%%%%%%%%%%%%%%%%%%%%%%%%%%%%%%%%%%%%%%%%%%%%
function c_out = radial_gouy(c_in, q_in)

%Determine the size of c_in and initialize an output array.
size = size(c_in,1);

```

```

c_out = zeros(size,1);

%Decompose the unmodified q term into z and Zr terms
z=real(q_in);
z_R = imag(q_in);
%This is the Gouy phase factor.
phi_g = atan(z/z_R);

%Apply the Gouy phase to all Laguerre-Gauss amplitudes calculated in
%<radial_lens.m>.
for k=1:size
    c_out(k) = c_in(k)*exp(-i*2*(k-1)*phi_g);
end

%%%%%%%%%%%%%%%%%%%%%%%%%%%%%%%%%%%%%%%%%%%%%%%%%%%%%%%%%%%%%%%%%%%%%%%%
%Subroutine :radial_correc.m
%Thermal lensing subroutine implementing the phase shift
%due to the second crystal (FK51 glass)
%Input variables:c_in,q_in, num_step, delta, Lambda,
%                lambda (see above)
%Output variables: c_out: Amplitude coefficients
%%%%%%%%%%%%%%%%%%%%%%%%%%%%%%%%%%%%%%%%%%%%%%%%%%%%%%%%%%%%%%%%%%%%%%%%
function c_out =
    radial_correc(c_in,q_in, num_step, delta, Lambda,lambda)

```

```

%Initialize the output variable
c_out = 0;

%Determine the new beam radius and curvature
w = sqrt(-lambda/(pi*imag(1/q_in)));
inv_R = real(1/q_in);

%Initialize radial coordinate
r = delta/num_step;

%Calculate the overlap integral of the compensated beam
%with the original
Gaussian amplitude profile. Then, report the overlap amplitude.
for step=1:num_step

    y = 2*r^2/w^2;
    LG(1) = 1;
    LG(2) = 1-y;
    LG(3) = (2-4*y+y^2)/2;
    for n=3:19
        LG(n+1) = ((2*n-1-y)*LG(n)-(n-1)*LG(n-1))/n;
    end

v_0 = (2/pi)^(1/2) * 1/w *exp(-r^2/w^2);

u_0 = v_0*LG(1)*exp(i*2*pi*Lambda(step)/lambda);
u_1 = v_0*LG(2)*exp(i*2*pi*Lambda(step)/lambda);
u_2 = v_0*LG(3)*exp(i*2*pi*Lambda(step)/lambda);

```

```

u_3 = v_0*LG(4)*exp(i*2*pi*Lambda(step)/lambda);
u_4 = v_0*LG(5)*exp(i*2*pi*Lambda(step)/lambda);
u_5 = v_0*LG(6)*exp(i*2*pi*Lambda(step)/lambda);
u_6 = v_0*LG(7)*exp(i*2*pi*Lambda(step)/lambda);
u_7 = v_0*LG(8)*exp(i*2*pi*Lambda(step)/lambda);
u_8 = v_0*LG(9)*exp(i*2*pi*Lambda(step)/lambda);
u_9 = v_0*LG(10)*exp(i*2*pi*Lambda(step)/lambda);
u_10 = v_0*LG(11)*exp(i*2*pi*Lambda(step)/lambda);
u_11 = v_0*LG(12)*exp(i*2*pi*Lambda(step)/lambda);
u_12 = v_0*LG(13)*exp(i*2*pi*Lambda(step)/lambda);
u_13 = v_0*LG(14)*exp(i*2*pi*Lambda(step)/lambda);
u_14 = v_0*LG(15)*exp(i*2*pi*Lambda(step)/lambda);
u_15 = v_0*LG(16)*exp(i*2*pi*Lambda(step)/lambda);
u_16 = v_0*LG(17)*exp(i*2*pi*Lambda(step)/lambda);
u_17 = v_0*LG(18)*exp(i*2*pi*Lambda(step)/lambda);
u_18 = v_0*LG(19)*exp(i*2*pi*Lambda(step)/lambda);

U_0 =
c_in(1)*u_0+c_in(2)*u_1+c_in(3)*u_2+c_in(4)*u_3+c_in(5)*u_4+c_in(6)*u_5+c_in(7)
*u_6+c_in(8)*u_7+c_in(9)*u_8+c_in(10)*u_9+c_in(11)*u_10+c_in(12)*u_11+c_in(13)*u
_12+c_in(14)*u_13+c_in(15)*u_14+c_in(16)*u_15+c_in(17)*u_16+c_in(17)*u_16+c_in(1
8)*u_17+c_in(19)*u_18;

c_out = c_out+ conj(v_0) * U_0* r*delta/num_step;

```



## REFERENCES

- [1] Timothy Ferris, *Coming of Age in the Milky Way*, Doubleday, New York, NY, 1989.
- [2] Bernard F. Schutz, *A First Course in General Relativity*, Cambridge University Press, Cambridge, UK, 1999.
- [3] Charles W. Misner, Kip S. Thorne, and John A. Wheeler, *Gravitation*, W. H. Freeman and Co., New York, NY, 1997.
- [4] V. Ferrari, “First Virgo-SIGRAV school on gravitational waves: Sources,” Seminar at Virgo detector facility in Cassina, Italy, May 2002.
- [5] Ronald Lane Reese, *University Physics*, Brooks/Cole Publishing Co., Pacific Grove, CA, 2002.
- [6] Bradley W. Carroll and Dale A. Ostlie, *An Introduction to Modern Astrophysics*, Addison-Wesley Publishing Company, Inc., Reading, MA, 1996.
- [7] B. Bertotti, “First Virgo-SIGRAV school on gravitational waves: Weak gravitational waves,” Seminar at Virgo detector facility in Cassina, Italy, May 2002.
- [8] Tom Delker, *Demonstration of a Prototype Dual-Recycled Cavity-Enhanced Michelson Interferometer for Gravitational Wave Detection*, Ph.D. dissertation, University of Florida, 2001.
- [9] C. Bradaschia, R. Delfabbro, A. Divirgilio, A. Giazotto, H. Kautzky, V. Montelatici, D. Passuello, A. Brilliet, O. Cregut, P. Hello, C.N. Mann, P.T. Manh, A. Marraud, D. Shoemaker, J.Y. Vinet, F. Barone, L. Difiore, L. Milano, G. Russo, J.M. Aguirregabiria, H. Bel, J.P. Duruisseau, G. Lederman, P. Tourrenc, M. Capozzi, M. Longo, M. Lops, I. Pinto, G. Rotoli, T. Damour, S. Bonazzola, J.A. Marck, Y. Gourghoulon, L.E. Holloway, F. Fuligni, V. Iafolla, and G. Natale, “The VIRGO Project - a wide band antenna for gravitational-wave detection,” *Nuclear Instruments and Methods in Physics Research A*, vol. 289, pp. 518–525, 1990.
- [10] A. Rüdiger, “The GEO 600 gravitational wave detector. Status, research, development,” in *Euro-Japan Seminar on Gravitational Wave Detection*, Tokyo, Japan, 1998, pp. 1–8.
- [11] A. Abramovici, W.E. Althouse, R.W. Drever, Y.Gursel, S. Kawamura, F.J. Raab, D. Shoemaker, L. Sievers, R.E. Spero, K.S. Thorne, R.E. Vogt,

- R. Weiss, S.E. Whitcomb, and M.E. Zucker, “LIGO: The Laser Interferometer Gravitational-Wave Observatory,” *Science*, vol. 256, pp. 325–333, 1992.
- [12] B.C. Barish and R. Weiss, “LIGO and the detection of gravitational waves,” *Physics Today*, pp. 44–50, 1999.
- [13] K. Tsubono, “300-m laser interferometer gravitational wave detector (TAMA 300) in Japan,” in *Proceedings of First Eduardo Amaldi conference on gravitational wave experiments, Frascati, Roma, June 1994*, Singapore, 1995, pp. 112–114, World Scientific.
- [14] Norman Hodgson and Horst Weber, *Optical Resonators: Fundamentals, Advanced Concepts, and Applications*, Springer-Verlag, London, UK, 1997.
- [15] Justin Mansell, Joeseeph Hennawi, Eric K. Gustafson, Martin M. Fejer, Robert L. Buyer, David Clubley, Sanichiro Yoshida, and David H. Reitze, “Evaluating the effect of transmissve optics thermal lensing on laser beam quality with a Shack-Hartmann wave-front sensor,” *Applied Optics*, vol. 40, pp. 366–370, 2001.
- [16] H. Luck, K.-O. Muller, P. Aufmuth, and K. Danzmann, “Correction of wavefront distortions by means of thermally adaptive optics,” *Optics Communications*, vol. 175, pp. 275–287, 2000.
- [17] K.A. Strain, K. Danzmann, J. Mizuno, P.G. Nelson, A. Rudiger, R. Schilling, and W. Winkler, “Thermal lensing in recycling interferometric gravitational wave detectors,” *Physics Letters A*, vol. 194, pp. 124–132, 1994.
- [18] W. Winkler, K. Danzmann, A. Rüdiger, and R. Schilling, “Heating by optical absorption and the performance of interferometric gravitational-wave detectors,” *Physical Review A*, vol. 44, pp. 7022–7036, 1991.
- [19] Patrice Hello and Jean-Yves Vinet, “Analytical models of thermal aberrations in massive mirrors heated by high power laser beams,” *J. Physique France*, vol. 51, pp. 1267–1282, 1990.
- [20] Guido Müller, Rupal S. Amin, Dave Guagliardo, Donovan McFeron, Ramsey Lundock, David H. Reitze, and D. B. Tanner, “Method for compensation of thermally induced modal distortions in the input optical components of gravitational wave interferometers,” *J. Classical and Quantum Gravity*, vol. 19, pp. 1793–1801, 2002.
- [21] M. P. MacDonald, Th. Graf, J.E. Balmer, and H.P. Weber, “Reducing thermal lensing in diode-pumped laser rods,” *Optics Communications*, vol. 178, pp. 383–393, 2000.
- [22] Grant R. Fowles, *Modern Optics*, Dover Publications, New York, NY, second edition, 1989.

- [23] Charles Kittel, *Introduction to Solid State Physics*, John Wiley and Sons, Inc., New York, 1996.
- [24] Christopher C. Davis, *Lasers and Electro-Optics: Fundamentals and Engineering*, Cambridge University Press, Cambridge, UK, 2000.
- [25] Antonello Cutolo, Paolo Gay, and Salvatore Solimeno, “Mirror deformations and wavefront aberrations caused by c.w. high power laser beams,” *Optica Acta*, vol. 27, pp. 1105–1116, 1980.
- [26] Schott Glass Technologies Inc., *Optical Glass Product Catalog*, Schott Glass Technologies Inc., Duryea, Pennsylvania, c1995.
- [27] Anthony E. Siegman, *Lasers*, University Science Books, Sausalito, CA, 1986.
- [28] H. Kogelnik and T. Li, “Laser beams and resonators,” *Applied Optics*, vol. 5, pp. 1550–1566, 1966.
- [29] A. Walther, *The Ray and Wave Theory of Lenses*, Cambridge University Press, Cambridge, UK, 1995.

## BIOGRAPHICAL SKETCH

Rupal Shashi(kant) Amin was born in Leeds, England, on May 20, 1977. His family soon relocated in the U.S.A. to pursue careers in chemistry and banking. Rupal entered the Florida Institute of Technology in 1995 as an aerospace engineer. However, he moved into physics two years later as he followed his father's scientific bent. At Florida Tech, Rupal had the fortune of working in several physics labs. His advisors and mentors Drs. Ryne Raffalle, Hamid K. Rassoul, and Mark Moldwin helped him on his meandering path through numerical and experimental physics. It was also at Florida Tech where Rupal obtained his first experience with NASA and extended duration microgravity experiments.

After graduating with honors, Rupal entered the University of Florida. A tough first year led him to the door of Drs. David B. Tanner and David Reitze. Under the scholarly advice of these professors, Rupal entered the LIGO project and began working with Dr. Guido Müller in high power experiments. These experiments led to a paper, attendance at professional conferences, new colleges, trips to the European detectors, and this thesis.